Contributions to Mineralogy and Petrology (2023) 178:68
https://doi.org/10.1007/s00410-023-02050-8

ORIGINAL PAPER

Compositional changes in garnet: trace element transfer during eclogite-facies metamorphism

Jan Kulhánek[1] · Shah Wali Faryad[1]

Received: 16 March 2023 / Accepted: 24 August 2023 / Published online: 11 September 2023

Abstract

The compositional zoning of the major divalent cations in metamorphic garnet is a useful tool in reconstructing the pressure–temperature path. However, trace elements can provide a better-preserved record of petrogenetic evolution due to their strong affinity in garnet and slow diffusion rates. In this study, three high-pressure micaschist samples of varying composition and garnet textures from the Krušné hory Mountains (Saxothuringian zone, Bohemian Massif) were examined. By utilizing electron probe micro-analysis and laser ablation inductively coupled plasma mass spectrometry, three distinct types of compositional zoning in garnet were identified by compositional mapping. The zoning types were classified as continuous core-to-rim change, concentric annular changes, and overprinting of a pre-existing distribution; all three provide information on the original mineral composition and texture before garnet overgrowth. The transition from overprint to annular zoning shows relation to temperature increment. The annular zoning allowed the identification of several coupled substitutions, including alkali (sodium and lithium) + yttrium and the alkali + phosphorus substitution which is typical of high- to ultra-high-pressure conditions. The formation of annuli zoning was interpreted to originate not only from the decomposition of trace element bearing phases, but also to be related to the availability of fluid medium during garnet growth. Two samples contained atoll texture garnets, interpreted to be originated from the dissolution of the garnet central part, chemically distinct from the new garnet growing coevally on the rim or replacing the original central part. This proposed process is evidenced by the mass balance calculation of yttrium and heavy rare earth elements between the dissolved garnet and newly formed parts.

Keywords Atoll garnet · Compositional mapping · LA-ICP-MS · Mass balance · Metamorphic garnet · Trace elements

Introduction

Garnet, as a common metamorphic phase stable in a wide range of pressure and temperature (PT) conditions, is typically used for constraining the metamorphic history of rocks. Recently, attention has been focused on the distribution of a wide range of trace elements in garnet that help to reconstruct various metamorphic processes during garnet growth or subsequent compositional alterations (Rubatto et al. 2020; Gaidies et al. 2021; Goncalves et al. 2021; Kulhánek et al. 2021; Aygül et al. 2022; Godet et al. 2022; Konrad-Schmolke et al. 2023). In addition to major elements, studies have mainly focused on the distribution of Y and rare earth elements (REE), especially heavy REE (HREE), which, among other metamorphic phases, enter garnet dominantly and have a very low diffusion coefficient (Otamendi et al. 2002; Tirone et al. 2005; Carlson et al. 2014). This allows for significantly better preservation of the original Y + HREE content of the garnet compared to divalent major elements.

This study focuses on a compositional and textural development of almandine-rich garnets with prograde zoning from high-pressure (HP) metapelites, among which some have well-developed garnet "atoll" textures. The atoll texture is represented by a concentric garnet rim (or ring) that is filled with a central "lagoon" of other minerals and possibly with garnet "islands" or "peninsulas" inside the atoll (Williamson 1934). The formation of the atoll texture in garnet remains a topic of ongoing scientific discourse, with multiple proposed mechanisms being considered. The key

Communicated by Daniela Rubatto.

✉ Jan Kulhánek
jan.kulhanek@natur.cuni.cz

[1] Faculty of Science, Institute of Petrology and Structural Geology, Charles University, Albertov 6, 128 43, Prague 2, Czech Republic

processes implicated in the possible formation of atoll texture encompass: (1) partial dissolution and replacement of the garnet crystal inner parts and possible accompaniment by the reprecipitation of garnet (Rast 1965; Smellie 1974; Homam 2003; Cheng et al. 2007; Galuskina et al. 2007; Faryad et al. 2010; Ruiz Cruz 2011; Jonnalagadda et al. 2017; Giuntoli et al. 2018; Kulhánek et al. 2021; Massonne and Li 2022); (2) the occurrence of multiple simultaneous nucleation and subsequent coalescence of garnet crystals (Spiess et al. 2001; Dobbs et al. 2003); (3) the presence of large amounts of matrix phases that exert dominance over specific internal regions within the poikiloblastic garnet grain (Atherton and Edmunds 1966; Ushakova and Usova 1990; Robyr et al. 2014; Godet et al. 2022); and (4) the gradual coalescence of garnet in intergranular space amid matrix phases (de Wit and Strong 1975). The formation of atoll garnets from adjacent metabasites was proposed as the gradual dissolution of compositionally stepwise distinct central parts from a concurrently growing new garnet at the rim, or by replacing the original garnet in the central part (Faryad et al. 2010; Kulhánek et al. 2021). To test such a process, the Y + REE mass balance between the potentially dissolved and newly grown garnet parts was calculated, showing that the amount of Y + HREE released during possible dissolution of the older central part of the garnet was incorporated into the competitively growing new garnet (Kulhánek et al. 2021). Such a process may then be related to the stepwise increase in Li, Na, Y, and HREE and to annular oscillations in Ca and Mn abundances in the garnet rim, observed also in the atoll garnets of micaschist samples. In this study, to decipher possible evidence of the atoll garnet formation process in the studied micaschists, the compositional distribution of trace elements, especially of Y + REE in atoll garnets, was examined in detail, including the calculation of mass balance.

Apart from the atoll garnets, different types of major and trace element zoning can also be observed in large porphyroblasts of "full" garnet. Here, using detailed compositional mapping by electron probe micro-analysis (EPMA) and laser ablation-inductively coupled mass spectrometry (LA-ICP-MS), the study identified three types of compositional zoning patterns: (1) continuous change (increase or decrease), (2) concentric annular changes, or (3) overprinting of a pre-existing distribution—inherited from precursor minerals. The continuous core-to-rim change is commonly well-observable among the major divalent elements in garnet and all zoning types can be formed in mutual combination. The characterization of different zoning patterns exhibited by trace elements in garnet and the underlying processes responsible for their formation have been extensively investigated in numerous studies, considering a wide range of factors that influence these processes (e.g., Pyle and Spear 1999; Konrad-Schmolke et al. 2008b; Moore et al. 2013; Raimondo et al. 2017; George et al. 2018; Rubatto et al. 2020; Konrad-Schmolke et al. 2023). The contribution of trace elements to garnet from other phases through metamorphic reactions is commonly associated with PT changes, although not exclusively. The PT variations can favor specific trace element substitutions with major elements, based on their relative energetics (e.g., Yang et al. 1999; Cahalan et al. 2014; Carlson et al. 2014). For example, Yang et al. (1999) found that the partitioning of Co and Zn between garnet and biotite is mainly temperature dependent, while Sc distribution was not affected by temperature. In addition, the pressure-dependent occurrence of phosphorus (P) coupled substitution with alkalis (Li, Na) in the garnet structure was established through calculations and experiments under HP to ultra-HP (UHP) conditions (Thompson 1975; Brunet et al. 2006; Hanrahan et al. 2009a; Konzett and Frost 2009). The partitioning of garnet structure preferring elements, particularly Mn, Y, and HREE, in garnet is then strongly influenced by several other distribution factors, such as the Rayleigh fractionation (Hollister 1966; Otamendi et al. 2002), diffusion-limited uptake from the matrix (Skora et al. 2006), decomposition of trace element bearing phases (e.g., Pyle and Spear 1999; Konrad-Schmolke et al. 2008a, b; Raimondo et al. 2017; Rubatto et al. 2020; Gaidies et al. 2021), grain boundary and microtopographic controls (Dempster et al. 2020), varying growth rates of garnet (George et al. 2018), infiltration of an externally derived fluid (Jamtveit et al. 1993; Dziggel et al. 2009; Moore et al. 2013), changes in the fluid transport permeability (Konrad-Schmolke et al. 2023), and garnet dissolution and reprecipitation process (Jedlicka et al. 2015; Dempster et al. 2017; Viete et al. 2018; Kulhánek et al. 2021). In low- to mid-temperature (LT–MT) conditions, less mobile elements such as Cr, Ca, Ti, Nb, and some of the REE (Sm, Eu, Gd, Tb) exhibit an overprint distribution in garnet when phases relatively rich in these elements are replaced by garnet (Yang and Rivers 2001; George et al. 2018). This behavior provides a coarse indication of the temperature conditions during element entrapment and the composition and texture of the precursor matrix of the rock (Yang and Rivers 2001; Moore et al. 2013; Raimondo et al. 2017; George et al. 2018; Rubatto et al. 2020).

The objective of this study was to perform a comprehensive quantitative analysis of trace element mapping and profiling. It aimed to elucidate the mechanisms governing trace element coupled substitutions during garnet growth, investigate the factors influencing the formation of diverse zoning styles, establish a robust correlation between compositional zoning and potential changes in PT conditions, examine the composition of the precursor matrix, and propose a plausible model for the formation of atoll garnets along with the associated trace element transfer processes. Through the utilization of advanced analytical techniques, this study strives to

enhance our understanding of the intricate behavior of trace elements within garnet, thus providing valuable insights into the metamorphic evolution of the investigated samples.

Geological setting

The European Variscan Belt is exposed in its easternmost part in Central Europe, forming the Bohemian Massif (Fig. 1a), and extensive crystalline segment composed of four main tectonically separated domains. Two regional tectonic zones (the Saxothuringian and Moldanubian) of Variscan orogeny age (~ 380–320 Ma, Schulmann et al. 2009, 2014) are situated between two tectonic blocks with Proterozoic basement—the Brunovistulian (~ 2.2–0.55 Ga, Jastrzębski et al. 2021) and Teplá-Barrandian (~ 750–540 Ma, Hajná et al. 2011) and surround the Teplá-Barrandian block itself (Fig. 1b). The presence of HP and UHP metamorphic rocks, forming boudins or lenses in amphibolite- and granulite-facies rocks, is characteristic for the Saxothuringian and Moldanubian zones, whereas the Bohemian Massif blocks (Brunovistulian and Teplá-Barrandian) do not contain such rocks (see Faryad 2011).

The Saxothuringian Zone forms a SW–NE-trending belt containing metamorphic rocks that underwent various stages of PT evolution during the Variscan subduction of the Saxothuringian lower plate beneath the Teplá-Barrandian upper plate, followed by subsequent exhumation (Schäfer et al. 1997; Franke 2000; Willner et al. 2000; Kroner et al. 2007; Schulmann et al. 2014; Jeřábek et al. 2016; Peřestý et al. 2017, 2020; Konopásek et al. 2019; Maierová et al. 2021). The UHP conditions of Saxothuringian rocks are recorded by the presence of coesite or diamond in eclogite, gneisses, and granulites (Schmädicke et al. 1992; Nasdala and Massonne

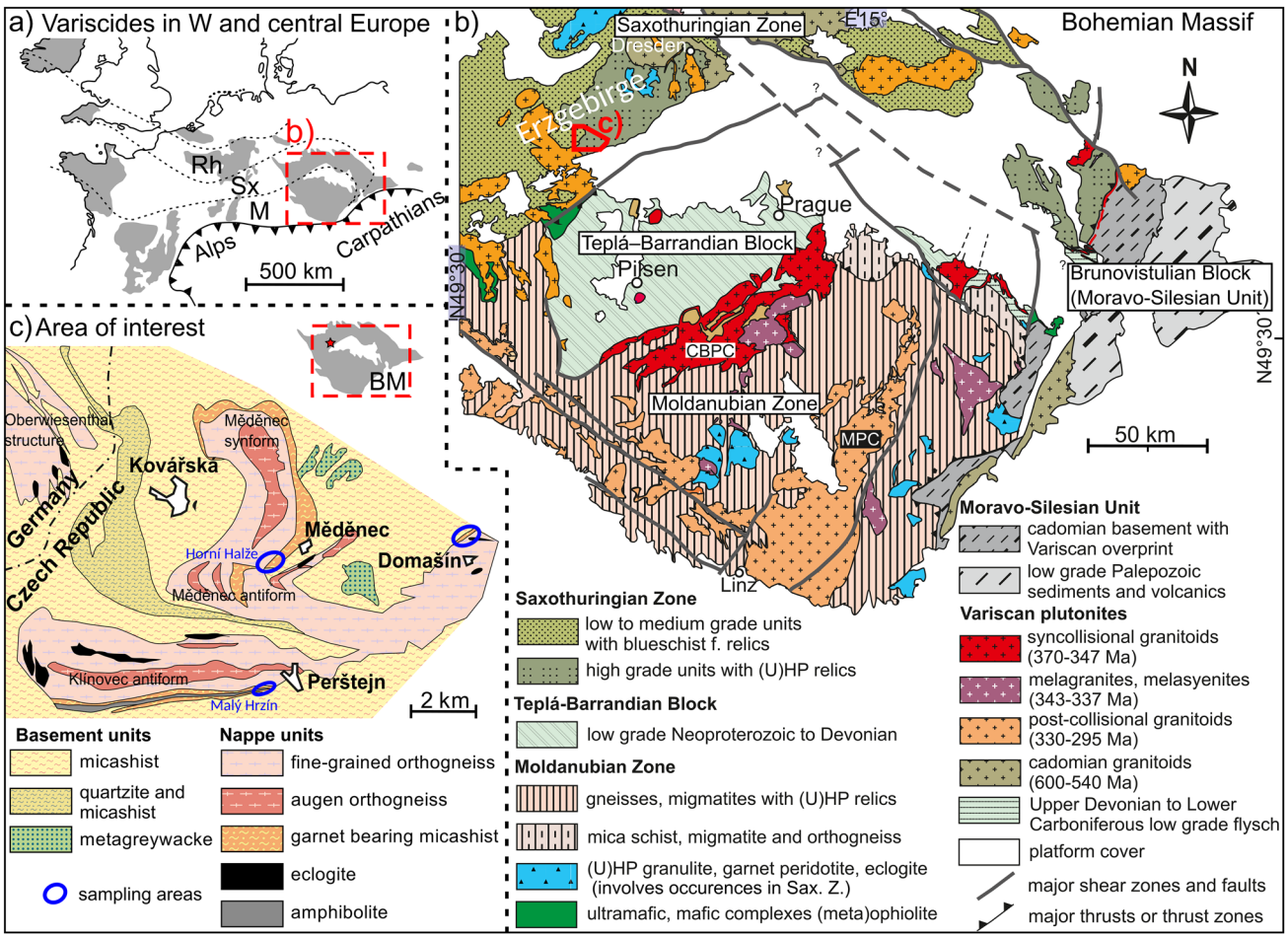

Fig. 1 **a** Sketch of the exposed Variscan orogenic belt in western and central Europe showing the position of the Bohemian Massif (Rh, Rheno-Hercynian Zone; Sx, Saxothuringian Zone; M, Moldanubian Zone). **b** Simplified geological map of the Bohemian Massif modified after Franke (2000) and Faryad and Kachlík (2013) showing the position of the study area. **c** Geological map enlargement of the central Erzgebirge (Krušné hory), modified after Konopásek (1998), with marked sampling locations. *CBPC* Central Bohemian Plutonic Complex, *MPC* Moldanubian Plutonic Complex

2000; Massonne 2001; Kotková et al. 2011; Kotková and Janák 2015; Závada et al. 2018, 2021) that are comparable with UHP rocks in the Moldanubian Zone (Medaris et al. 2006; Kobayashi et al. 2008; Faryad 2009; Perraki and Faryad 2014; Jedlicka et al. 2015; Haifler and Kotková 2016; Faryad and Cuthbert 2020). In addition to UHP rocks, a high number of HP eclogite- and blueschist-facies rocks have also been described from the Saxothuringian Zone (e.g., Klápová et al. 1998; Konopásek 2001; Massonne and Kopp 2005; Faryad 2012; Faryad and Kachlík 2013; Collett et al. 2017; Kulhánek et al. 2021; Jouvent et al. 2022).

The western part of the Saxothuringian Zone is referred as Erzgebirge or the Krušné hory Mts., which is an antiformal SW–NE-trending dome structure consisting of Cadomian para-autochthon basement overlain by several lithotectonic nappe units with unclear contacts (Rötzler et al. 1998; Willner et al. 2000; Konopásek et al. 2001; Konopásek and Schulmann 2005; Kroner et al. 2007; Collett et al. 2020; Kryl et al. 2021). The allochthonous nappe units that overthrusted the basement consist of high-grade metamorphic rocks with decreasing peak conditions lithostratigraphically from the lowermost units toward the top. In this order, the units are described as: the Cadomian basement, Gneiss–Eclogite Unit (GEU), Micaschist–Eclogite Unit (MEU), (Garnet)-Phyllite Unit, and several crystalline klippen (Münchberg, Wildenfels, and Frankenberg), collectively referred to as the uppermost allochthon. The Cadomian basement consists of medium pressure (MP)–high temperature (HT) Granite–Gneiss Amphibolite Unit with no evidence of HP metamorphism, referred also as red and grey gneiss unit (Kröner et al. 1995; Rötzler 1995; Mingram 1998; Rötzler et al. 1998; Willner et al. 2000; Kryl et al. 2021). As described by Kryl et al. (2021), the Gneiss–Eclogite Unit can be subdivided into GEU I (gneisses, migmatites, and eclogites), which underwent MP-HT peak conditions (Willner et al. 1997, 2002) and developed late exhumation contact with para-autochthonous Cadomian basement; and GEU II (diamond- and/or coesite-bearing gneisses, migmatites, granulites, and eclogites with lenses of garnet peridotites), which established early exhumation contact with the basement and recorded UHP-HT peak conditions (Schmädicke et al. 1992; Nasdala and Massonne 2000; Massonne and Nasdala 2003; Massonne and O'Brien 2003). Tectonic development with UHP-HT peak conditions similar to those of GEU II has been described for the rocks (diamond- and/or coesite-bearing gneisses, granulites, and migmatites) of the neighboring Eger Crystalline Complex (Konopásek and Schulmann 2005; Kotková et al. 2011; Haifler and Kotková 2016; Závada et al. 2018, 2021). The Micaschist–Eclogite Unit, from where the studied rock samples were sourced, is composed of chloritoid- and garnet-bearing micaschists together with occurrences of quartzites, marbles, and lenses or boudins of eclogites along the boundary between orthogneiss and micaschists (Konopásek 1998). The eclogite bodies vary in chemical and mineral composition (Klápová 1990; Klápová et al. 1998), but most of them have yielded similar peak conditions in the range of 2.5–2.7 GPa and 600–650 °C (Klápová et al. 1998; Faryad et al. 2010; Collett et al. 2017; Kulhánek et al. 2021), while some are interpreted to have reached even higher temperatures (e.g., 720 °C, Massonne and Kopp 2005). The HP–medium temperature (MT) estimates for micashists show a PT range of 2.3–2.6 GPa and 550–640 °C, similar to the eclogites, but lower peak pressure conditions of about 1.4–1.8 GPa were also calculated. This peak pressure range was interpreted to reflect the original positions (depths) of metapelites within the former orogenic wedge (Konopásek 2001; Jouvent et al. 2022). The peak pressure conditions for GEU and MEU are dated in the range of 350–340 Ma (Jouvent et al. 2023). The (Garnet)-Phyllite Unit is composed of chloritoid- and garnet-bearing phyllites and schists with intercalations of quartzites and metabasites with blue amphibole occurrences (Holub and Souček 1992; Rötzler et al. 1998; Faryad and Kachlík 2013; Jouvent et al. 2022). The garnet-bearing phyllite located in the vicinity to the rocks of MEU records HP conditions of up to 1.9 GPa (Jouvent et al. 2022).

For this study, micaschist samples were collected from three localities (Horní Halže, Malý Hrzín, and Domašín), in all cases in close vicinity with eclogite or amphibolite (retrogressed eclogite) bodies of MEU, which in that area form Měděnec and Klínovec antiform structures, together with gneisses of the GEU (Konopásek et al. 2001; Kryl et al. 2021; Fig. 1c). The coordinates of the sampling locations are given in the supplementary data Table 1S.

Analytical methods

In the laboratories of the Institute of Petrology and Structural Geology, Faculty of Science, Charles University and the Institute of Geology, Czech Academy of Sciences in Prague, polished thin sections of selected samples were analyzed. The analyses were performed using an electron probe micro-analyzer (EPMA)—JEOL JXA-8530F equipped with five wavelength dispersive spectrometers. The backscattered electron (BSE) detectors installed on EPMA were used for imaging. Accurate mass fractions in parts per million (ppm) were obtained using laser ablation inductively coupled plasma mass spectrometry (LA-ICP-MS), employing a Thermo Fisher Scientific Element 2 ICP-MS system with a 213 nm ablation laser system (Nd YAG UP-213, New Wave Research).

The EPMA was employed for quantitative chemical spot analyses, which were acquired using the associated wavelength dispersive spectrometers (WDS) under specific operating conditions. Conditions for quantitative analyses

included an accelerating voltage of 15 kV, a beam current of 30 nA, peak/background count times of 30/15 s, and the ZAF correction procedure. The diameter of the electron beam used for measurements ranged from 1 to 10 µm, depending on the mineral phase being analyzed. Furthermore, high-resolution compositional mapping of major and trace elements was conducted using the EPMA with an accelerating voltage of 20 kV, a beam current of 120 nA, a dwell time of 50 ms, and a step size of 1–7 µm. The EPMA used a set of standards for calibration, including Na—albite, Mg—periclase, Al—corundum, Si—quartz, P—apatite, K—sanidine, Ca—calcite, Ti—rutile, V—vanadinite, Cr—chromium oxide, Mn—rhodonite, Fe—magnetite, Zn—willemite, Y—yttrium–aluminum garnet (YAG), and Ba—baryte.

The contents of various trace elements in garnet, phengite, paragonite, chlorite, apatite and staurolite were quantified using LA-ICP-MS. Circular spots with a diameter of 40 – 50 µm or transects with a linear raster of 20 – 25 µm beam size, 60 µm raster length, and 1 µm s^{-1} scan speed were used to ablate selected areas in mineral grains. The laser was fired at a repetition rate of 10 Hz with a fluence of 11 J cm^{-2}. The time-resolved signal data were processed using Glitter software (van Achterbergh et al. 2001). Calibration was performed using the NIST SRM 612 standard (Jochum et al. 2011) and internal standardization was achieved by utilizing the 43Ca method. This was normalized relative to a stoichiometric internal standard isotope in the reference material, using data measured by EPMA (WDS) to avoid obtaining irregularities in the grain structure. The relative standard deviation of the laser ablation analyses was up to 5% for most of the detected elements. The detection limit was derived through multiplication of the background measurement variance, based on counting statistics, by a factor of 3.25, and expressed in counts. Elemental minimum detection levels were determined from this, which were then converted into concentrations using the yield ratio between the element of interest and the internal standard element in both the unknown and standard samples. The Glitter software routinely provides this approach, and it is elucidated in detail in the Glitter manual (van Achterbergh et al. 2005). The detection limits, expressed in ppm, for the isotopes analyzed in selected spots and transects are as follows (refers to certain isotope of element): ^{7}Li- 2; ^{85}Rb- 0.3; ^{88}Sr- 0.1; ^{89}Y- 0.1; ^{139}La- 0.01; ^{140}Ce- 0.01; ^{141}Pr- 0.01; ^{146}Nd- 0.05; ^{147}Sm- 0.05; ^{153}Eu- 0.02; ^{157}Gd- 0.1; ^{159}Tb- 0.05; ^{163}Dy- 0.05; ^{165}Ho- 0.02; ^{166}Er-0.05; ^{169}Tm - 0.02; ^{172}Yb - 0.05; ^{175}Lu - 0.02.

Aside from the 179 analyses performed on selected spots and transects, some of which were included in the compositional profiles of garnet, a compositional trace element map was also obtained using LA-ICP-MS. To generate the map, point analyses were conducted using a beam size diameter and step size of 50 µm, which sequentially mapped a rectangular field measuring 13.2 × 11.2 mm, encompassing the garnet porphyroblast. The mean detection limits, expressed in ppm, for the isotopes utilized in mapping are as follows: ^{7}Li—0.28; ^{23}Na — 0.28; ^{47}Ti — 0.84; ^{51}V — 0.03; ^{53}Cr — 0.37; ^{59}Co — 0.02; ^{66}Zn — 0.15; ^{85}Rb — 0.08; ^{88}Sr — 0.01; ^{89}Y — 0.01; ^{90}Zr — 0.01; ^{93}Nb — 0.01; ^{139}La — 0.01; ^{140}Ce — 0.01; ^{141}Pr — 0.01; ^{146}Nd — 0.01; ^{147}Sm — 0.01; ^{153}Eu — 0.01; ^{157}Gd — 0.01; ^{159}Tb — 0.01; ^{163}Dy — 0.01; ^{165}Ho — 0.01; ^{166}Er — 0.01; ^{169}Tm — 0.01; ^{172}Yb — 0.01; ^{175}Lu — 0.01. The measured isotopes ^{45}Sc and ^{71}Ga cannot provide quantitatively reliable analysis due to peak overlay with analyzed major elements. Nonetheless, these isotopes can still be utilized to display changes in zoning on a relative scale. The data processing of the mapped area in the thin section, as well as the subsequent image analysis, were executed using the Python programming language. To present the compositional profiles and derive the corresponding summary values from distinct parts of the garnet that would not be influenced by values from inclusions or phases filling the garnet fractures, masks were generated utilizing the Python programming language. These masks delineated the desired parts of the garnet. Garnet compositional profiles can combine the display of elements measured by LA-ICP-MS and EPMA (mainly P).

In accordance with Warr (2021), abbreviations for mineral phases were used in this study. The article mentions elements in the form of element symbols. Garnet endmembers were determined as follows: Alm (almandine) = 100 Fe^{2+} / (Fe^{2+} + Mg + Ca + Mn); Prp (pyrope) = 100 Mg / (Fe^{2+} + Mg + Ca + Mn); Grs (grossular) = 100 Ca / (Fe^{2+} + Mg + Ca + Mn); and Sps (spessartite) = 100 Mn / (Fe^{2+} + Mg + Ca + Mn), and were reported in terms of mole percent (mol %). Additionally, the ratio between the contents of Fe^{2+} and Mg was calculated as X_{Mg} = 100 Mg / (Mg + Fe^{2+}). To determine the andradite component, the charge balance of the calculated garnet formulae was employed. However, the results of the analysis indicated that no or only a negligible amount of andradite component was detected. The representation of elements in minerals can also be given in the study as number of atoms per mineral formula unit (a.p.f.u.).

Results

Petrography of studied micaschists

The micaschists consist of quartz, white mica (muscovite, phengite, paragonite), plagioclase, and garnet. Small amounts of prograde chloritoid, kyanite, ilmenite, rutile, and retrograde biotite, ilmenite, chlorite, staurolite, and epidote are also commonly present. Zircon, apatite, monazite, allanite, florencite, titanite, and tourmaline can be observed

among accessory phases. The foliation is defined by the alternating bands, ribbons, or lenticular domains of micas and quartz (Fig. 2). Garnet forms porphyroblasts which can reach up to 15 mm in diameter. They may have helicitic and snow-ball inclusion textures. An atoll garnet texture filled with chlorite, biotite, and quartz is also common. Texturally and compositionally different samples from three localities (JK2-19 Horní Halže; JK22-20 Malý Hrzín; F16-07 Domašín) were selected for more detailed analysis.

Micaschist Horní Halže

Larger lenticular domains of quartz and white mica (Fig. 2a), with a low amount of garnet (0.5–2 mm in diameter) are common in micaschists from Horní Halže (JK2-19). Garnet frequently shows net-like texture created by growth at a high angle to quartz grain boundaries (Fig. 3a, b), where the garnet is more easily replaced by retrograde biotite and chlorite. The atoll texture of garnet is also common, evidenced by a rim of garnet enveloping lagoons of other minerals (Fig. 3a). Rarely, the remaining garnet islands occur in the lagoons composed mainly of quartz inside the atoll garnet (Figs. 2b; 3c). The quartz in lagoons contains a high number of garnet and fluid inclusions (Fig. 2c). The retrograde chlorite and biotite surround garnet porphyroblasts and grow well in the pressure shadows. Small rutile grains are mostly fully replaced by ilmenite. Retrograde epidote is rarely present in matrix.

Micaschist Malý Hrzín

The micaschist from Malý Hrzín (sample JK22-20) is typically dominated by coarser texture with large porphyroblasts of garnet (up to 15 mm in diameter) which are surrounded by ribbons and lenticular domains of quartz and muscovite/phengite (Figs. 2e, f; 3d). The garnets may be continuously replaced by chlorite and biotite (Fig. 2g) or have a nearly untouched rounded shape (Fig. 2h). Often

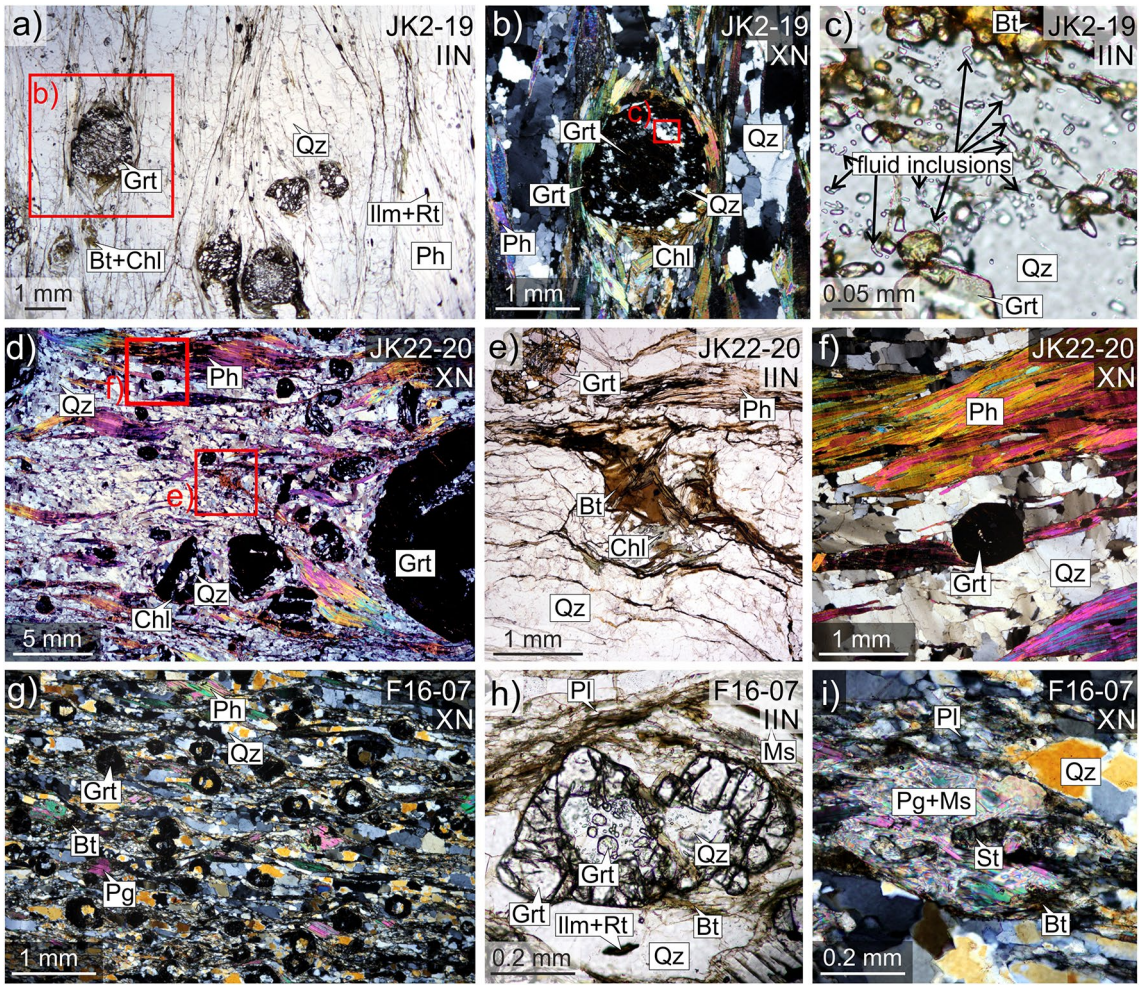

Fig. 2 Microphotographs from the optical microscope in parallel (IIN) and crossed (XN) polarizers; **a–c** sample JK2-19; **d–f** sample JK22-20; **g–i** sample F16-07

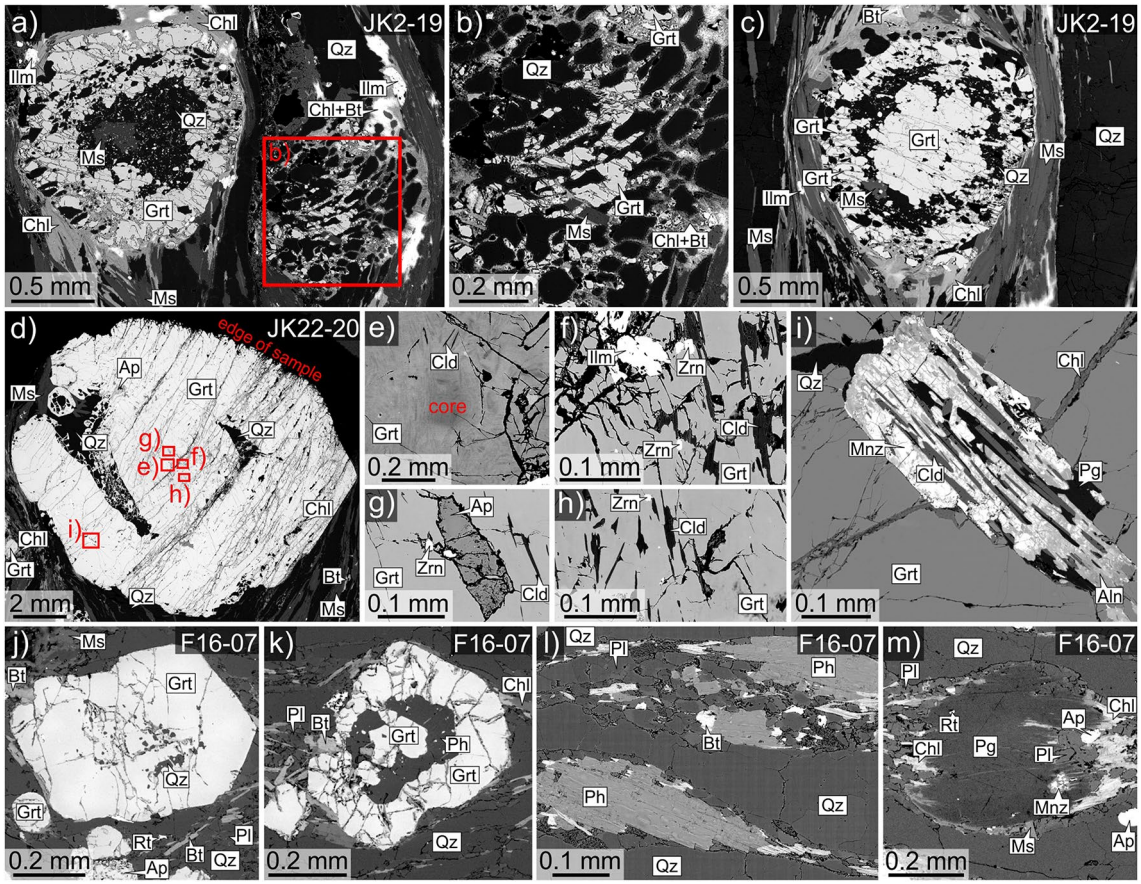

Fig. 3 BSE images of studied samples **(a–c)** JK2-19, **(d–i)** JK22-20, and **(j–m)** F16-07; **a** atoll garnet with quartz and muscovite "lagoon" and nearly fully replaced garnet by phyllosilicates and quartz, with detail on **(b)**; **c** atoll garnet with garnet "island" inside quartz lagoon; **d** large well-preserved porphyroblast of garnet with numerous inclusions (chloritoid, zircon, ilmenite, phosphates, allanite, and paragonite) and fractures filled mainly by chlorite, in detail on **(e–i)**; **j** well-preserved porphyroblast of garnet with numerous inclusions of quartz; **k** atoll garnet with garnet island inside surrounded by quartz and mica lagoon; **l** tabular grains of phengite (zonal development of phengitic component) in association with the plagioclase and biotite forming elongated lenticular shape bands; **m** paragonite porphyroblast surrounded by thin layer of muscovite and with chlorite and plagioclase in the pressure shadows, contains also monazite and rutile inclusions, apatite in the vicinity of the grain

visible are quartz bands overgrown by garnet (in some cases, rotated in) and garnet growing in the intergranular space of quartz (Fig. 3d). A high number of inclusions of chloritoid, zircon, ilmenite, and rutile are distributed across garnet grains (Fig. 3e–h). Chloritoid and ilmenite are commonly present in the core and mantle parts of garnet and chloritoid forms elongated needles, which reflect the original texture of the matrix by their orientation. Small grains of zircon are present throughout whole garnet, and rutile is enclosed in the rim parts. Several phosphate inclusions (apatite, monazite, and florencite) together with allanite and paragonite are also present (Fig. 3g, i). Along fractures, garnet is mostly replaced by chlorite.

Micaschist Domašín

In micaschist from Domašín (sample F16-07), a high content of quartz dominates in the form of bands alternating with muscovite/phengite and paragonite or a small amount of plagioclase and biotite. The garnet content is higher than in other samples but forms smaller grains (mostly 0.3–0.5 mm in diameter, Fig. 2i, j). Well-preserved garnet contains high number of quartz inclusions in its core (Fig. 3j), but most garnet grains are fractured and form atoll textures (Figs. 2k; 3k). The lagoons of matrix minerals in atolls are most commonly filled by quartz. Islands and peninsulas of garnet are also present. Small garnet grains and fluid inclusions are frequently present in quartz lagoons. Paragonite associated

with muscovite forms small lenses together with a minor amount of staurolite grains (Fig. 2l). Phengite forms larger tabular grains with biotite on the edges and surrounded by plagioclase (Fig. 3l). Paragonite forms large (up to 0.6 mm) rounded grains, possibly pseudomorphs after jadeite, with common pressure shadows filled with chlorite, plagioclase, and muscovite (Fig. 3m). Rutile is partly or fully replaced by ilmenite and a small amount of larger apatite grains occur in the matrix. Small crystals of kyanite are rarely present.

Compositional changes in garnet

The employed techniques for measuring trace elements and their processing techniques varied among the samples, based on the specific compositional and textural features in each sample. This includes EPMA and LA-ICP-MS compositional profiling and mapping. A summary of the compositional core-to-rim changes of the major and trace elements of the garnet is given in Table 1.

Sample JK2-19 (Horní Halže)

According to EPMA maps of atoll garnets, two compositionally distinct types of garnets were identified, referred to as Grt I and Grt II. Grt I, located in the inner part of the garnet, is rich in Ca and Mn. On the other hand, Grt II, located at the rims of the garnet, has a higher concentration of Fe and Mg (as shown in Fig. 4a–e). In some cases, Grt II was also found growing inside the atolls and replacing Grt I (as shown in Fig. 4a). Interestingly, the inner Grt II was found to have a similar major element composition as the rim Grt II, with the exception of higher levels of Mn (full Ca-, Mg-, Fe-, and Mn-maps in the supplementary Fig. 1S). Furthermore, a noticeable annular increase in Y and Na was observed just behind the transition from Grt I to Grt II at the grain rims, as evident in the element maps (Fig. 4f, g).

A core-to-rim compositional profile was carried out on one atoll garnet grain with an island of residual Grt I and a quartz lagoon separating the atoll from the island parts. The rim of the garnet (atoll), which comprises Grt II on the outside and Grt I on the inside, can be distinguished by the Ca-map (as illustrated in Fig. 4b). The profile spots for the major elements, as measured by EPMA, were situated adjacent to the ablated spots analyzed by LA-ICP-MS, as shown in Fig. 4h and i. To achieve an accurate characterization of the core-to-rim development and avoid any confounding effects of inclusions and crack alterations, a total of 27 spots/transects were carefully selected for profiling. However, minor variations were observed in the profile (as depicted in Fig. 4j). The Grt I/II transition is recognizable by clear changes in the Ca, Fe, and Mg contents, as follows. A decrease in Mn and Ca and increase in Fe and Mg from core to rim in the profile indicate a possible prograde development during garnet growth (Sps 2.7 → 1.3; Grs 11.8 → 3.6; Alm 79 → 86.7; Prp 6.8 → 8.2%). Spatial variation in composition in central Grt I, and sharp enrichment in Mn and Ca (compensated by Fe and Mg decrease) are visible just before the Grt I/II transition (Sps 2.3–3.0; Grs 10.7–18.0; Alm 80.0–73.5; Prp 7.1–5.5%). At the very edge of the grain, a small enrichment by Ca (Grs 3.6 → 5.9%) compensated by Fe (Alm 86.7 → 85.1%) is also apparent.

Quantitative contents of trace elements (Li, Y, and REE) were measured by LA-ICP-MS along the profile of garnet (Fig. 4k–q). The REE values were normalized by chondrite composition, following Boynton (1984), and the results are shown in Fig. 4r. The core of the garnet, as identified by analysis spots n. 1–8 in the profile, is distinguished by a well-correlated abundance of Y, Li, HREE, and Ho, with the exception of spot n. 2. This deviation may be attributed to the analysis of an altered segment along the crack, as demonstrated in Fig. 4k–m and p. These elements exhibit a sharp decrease upon transition to analysis spot n. 9, and subsequently, show minimal fluctuations until the edge of the garnet island within the atoll (up to analysis spot n. 15). The Dy content exhibits only minor variations throughout the entire garnet island. However, the Gd and Tb of mid-heavy REE (MREEs—Gd, Tb, Dy, and Ho), as well as the Eu and Sm of light REE (LREE—La, Ce, Pr, Nd, Sm, and Eu), demonstrate slightly elevated values in the outer part of the garnet island (as observed in analysis spots n. 9–15; see Fig. 4p, q). The entire garnet grain shows low levels of Nd, and the LREE lighter than Nd were mostly found below the detection limit (as illustrated in Fig. 4r). A decrease in the content of Y, HREE, MREE, and Sm occurs with transitions to the atoll part of the grain, more specifically on a small protrusion where a variation in major element contents was also apparent (spot n. 16, 18). With the transition from Grt I into Grt II in the atoll part (spot n. 19–23), a narrow spike of Li, Y, HREE, MREE, and Eu with Sm is evident. In particular, the highest peaks are recorded by Li, Y, Ho, Dy, and Er in analysis spot n. 23 (Fig. 4k, n, o) and Tb, Gd, Eu, and Sm in analyses spots n. 20 and 21 (Fig. 4p, q). Close to the edge of the grain (spot n. 24), the contents of Y, HREE, Ho, Dy, and Tb drop sharply and remain low to the very edge of grain (spot n. 27). The content of Li records similar behavior, but the drop occurs one analysis spot later (spot n. 25). The contents of Gd, Eu, and Sm show short-wavelength fluctuations at the edge of grains.

Sample JK22-20 (Malý Hrzín)

One large porphyroblast of garnet with inclusions (Fig. 3d–i) was selected for a detailed study. The thin section of JK22-20 was prepared to ideally cut the core of this large garnet grain. The garnet partly encloses a quartz band, inside which the garnet also grew at the quartz grain boundaries,

Table 1 Quantitative chemical analyses of garnets showing different parts of garnet profiles of three samples; oxides measured by WDS on EPMA and expressed in weight percent and calculated on cations of crystal chemical formulas with 12 oxygens, X_{Mg} and garnet end-members; trace elements (Li, Rb, Sr, Y, and REE) measured by LA-ICP-MS and expressed in ppm, if not under detection limits (<DL); approximate data (~) extracted from several measured points of the compositional LA-ICP-MS maps

Sample:	JK2-19	JK2-19	JK2-19	JK2-19	JK22-20	JK22-20	JK22-20	F16-07	F16-07	F16-07	F16-07
Phase:	Grt I	Grt I	Grt II	Grt II	Grt I	Grt I/II	Grt II	Grt I	Grt I	Grt II	Grt II
Position:	Core	Rim	Peak rim	Rim	Core	Transition	Rim	Core	Rim	Rim	Island
SiO_2	37.25	36.56	36.38	36.12	36.96	36.64	37.29	36.91	36.93	37.14	38.18
TiO_2	<DL	0.076	<DL	0.034	0.17	0.34	0.035	0.017	0.044	0.026	<DL
Al_2O_3	20.06	20.64	20.52	20.45	20.49	20.72	20.66	21.01	21.03	21.23	21.62
FeO_{tot}	34.74	33.53	37.26	37.96	27.14	38.96	37.55	28.12	32.06	29.91	30.01
MnO	1.16	1.00	0.93	0.58	3.63	0.21	0.14	1.37	0.85	0.69	0.96
MgO	1.65	1.46	1.95	1.91	0.26	1.34	2.27	3.55	4.15	6.21	5.59
CaO	3.74	6.26	2.30	2.06	9.61	0.72	0.81	8.43	4.95	3.84	3.86
Na_2O	<DL	<DL	<DL	<DL	0.022	0.033	0.019	<DL	<DL	<DL	<DL
P_2O_5	<DL	<DL	<DL	<DL	0.036	0.13	0.090	<DL	<DL	<DL	<DL
Total	98.61	99.53	99.34	99.13	98.32	99.08	98.87	99.40	100.01	99.05	100.21
Si	3.05	2.97	2.98	2.97	3.02	3.01	3.04	2.95	2.95	2.96	3.00
Ti	<DL	0.0046	<DL	0.0021	0.010	0.021	0.0021	0.0010	0.0027	0.0016	<DL
Al	1.94	1.98	1.98	1.98	1.97	2.00	1.99	1.98	1.98	1.99	2.00
Fe^{3+}	<DL	<DL	<DL	<DL	<DL	<DL	<DL	<DL	<DL	<DL	<DL
Fe^{2+}	2.38	2.28	2.55	2.61	1.85	2.67	2.56	1.88	2.14	1.99	1.97
Mn	0.081	0.069	0.065	0.040	0.25	0.014	0.010	0.093	0.057	0.047	0.063
Mg	0.20	0.18	0.24	0.23	0.032	0.16	0.28	0.42	0.49	0.74	0.65
Ca	0.33	0.55	0.20	0.18	0.84	0.063	0.071	0.72	0.42	0.33	0.32
Na	<DL	<DL	<DL	<DL	0.0034	0.0052	0.0030	<DL	<DL	<DL	<DL
P	<DL	<DL	<DL	<DL	0.0025	0.0088	0.0062	<DL	<DL	<DL	<DL
Total	7.98	8.03	8.03	8.03	7.98	7.96	7.95	8.06	8.05	8.05	8.00
X_{Mg}	0.08	0.07	0.09	0.08	0.02	0.06	0.10	0.18	0.19	0.27	0.25
Alm	0.796	0.743	0.835	0.851	0.622	0.917	0.878	0.603	0.687	0.642	0.654
Prp	0.068	0.057	0.078	0.076	0.011	0.056	0.094	0.136	0.159	0.238	0.217
Grs	0.110	0.177	0.066	0.059	0.282	0.022	0.024	0.232	0.136	0.106	0.108
Sps	0.027	0.022	0.021	0.013	0.084	0.005	0.003	0.030	0.018	0.015	0.021
Li	31.45	7.14	58.03	25.80	~160	~80	~75	21.18	20.99	10.82	47.67
Rb	<DL	<DL	<DL	<DL	<DL	<DL	<DL	<DL	<DL	<DL	<DL
Sr	0.17	<DL	<DL	<DL	<DL	<DL	<DL	0.17	<DL	<DL	<DL
Y	750.1	37.97	1711.1	45.22	~2600	~30	~11	329.3	96.36	60.56	290.6
La	<DL	<DL	<DL	<DL	~0.1	~0.5	~0.2	<DL	<DL	<DL	<DL
Ce	0.04	0.02	<DL	<DL	~0.3	~2	~1	<DL	<DL	<DL	<DL
Pr	<DL	<DL	<DL	<DL	~0.03	~0.2	~0.05	<DL	<DL	<DL	0.03
Nd	0.15	0.14	0.22	0.08	~0.09	~1	~0.2	0.28	0.18	0.15	0.24
Sm	1.16	0.73	2.00	2.52	~0.1	~2	~1	1.74	1.24	1.32	1.19
Eu	0.77	0.93	1.38	1.84	~0.2	~1	~0.7	1.67	1.95	1.42	1.12
Gd	11.74	6.88	23.63	26.55	~3	~9	~6	9.94	14.13	12.07	7.91
Tb	5.01	1.54	14.73	4.87	~3	~4	~1	2.88	3.46	2.67	1.80
Dy	68.01	8.35	195.8	18.28	~100	~2.5	~4	32.72	20.25	13.94	18.49
Ho	25.10	1.21	57.17	1.86	~90	~11	~0.5	10.58	3.61	2.24	9.91
Er	127.7	2.57	168.3	3.11	~750	~8	~1.5	49.69	9.44	5.28	56.08
Tm	28.47	0.28	19.58	0.34	~270	~1	~0.15	9.37	1.14	0.72	11.94
Yb	285.0	1.13	100.0	2.59	~3200	~6	~1	77.29	7.05	4.71	104.2
Lu	71.12	0.11	13.13	0.58	~550	~1	~0.2	12.50	0.94	0.62	17.32

Position peak rim—peak Y concentrations at the rim part; transition—transition between Grt I and II; island—the island part inside atoll garnet

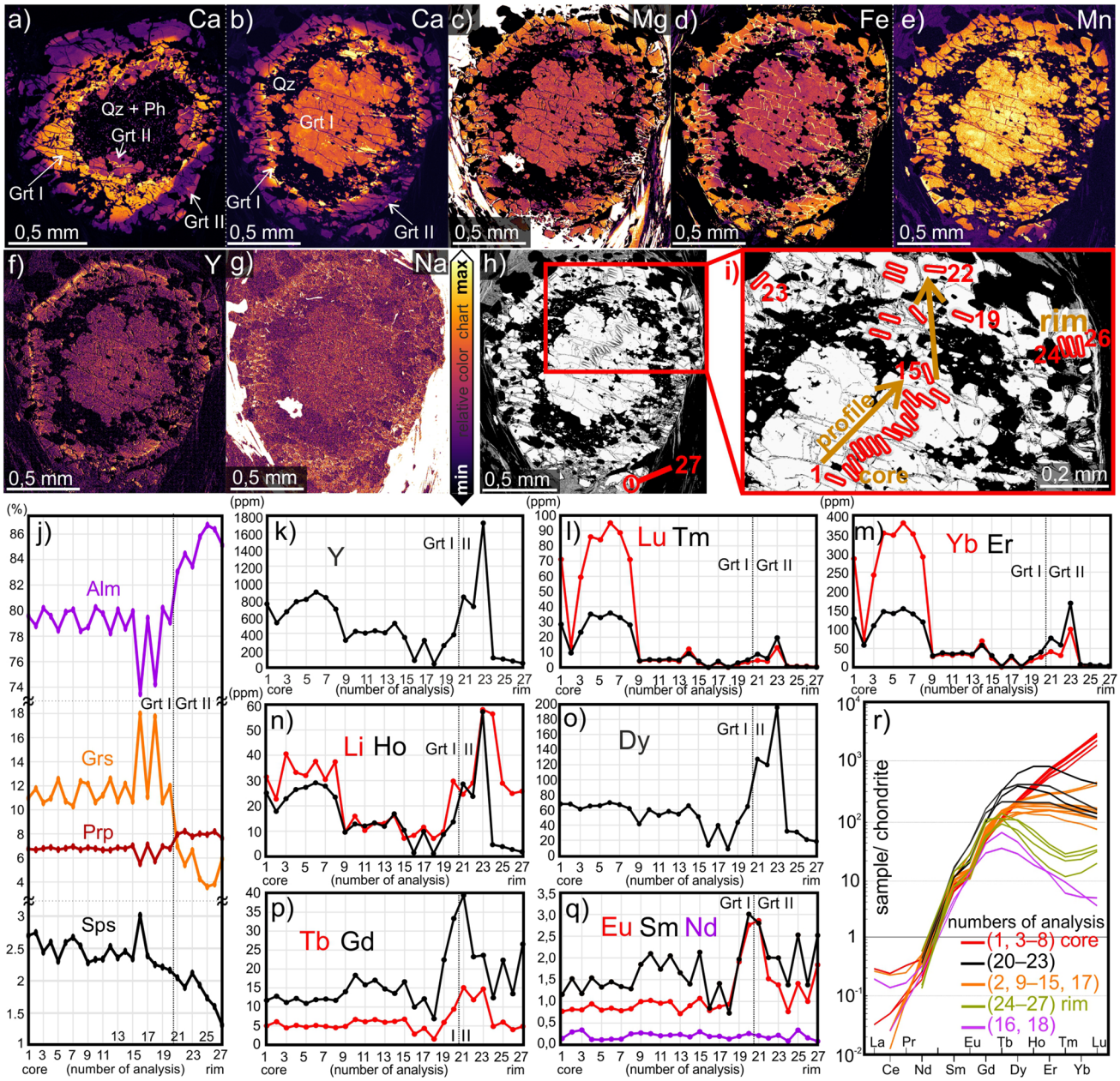

Fig. 4 **a–g** Compositional maps of major and trace elements in garnets of sample JK2-19 (measured by WDS on EPMA); **a** atoll garnet composed of Grt I (higher Ca) and Grt II (lower Ca); **b–g** atoll garnet with residual Grt I island inside and a lagoon of quartz separating it from the atoll part composed of Grt I and II; **h–i** BSE image of garnet with the positions of the analysis transects marked; **j** compositional profile of major elements of garnet, recalculated to garnet endmembers (measured by WDS on EPMA); **k–q** compositional profile of trace elements (Li + Y + REE) in garnet (measured by LA-ICP-MS); **r** profile of REE analyses normalized to the chondrite values of Boynton (1984)

forming a thin fish-net texture. The core-to-rim profile of the grain (Fig. 5a) was constructed using EPMA, and the trajectory was determined based on the compositional variations observed in the maps of major and trace elements obtained through EPMA (Fig. 5b–h). The profile displays major element contents recalculated to garnet endmembers (Fig. 5a). The core of garnet shows the lowest concentrations of Fe and Mg, compensated by the highest contents of Ca and Mn (Alm 62.2; Prp 1.1; Grs 28.2; Sps 8.5%; Fig. 5a). The garnet shows increasing Fe and Mg and decreasing Ca and Mn with bell-shaped distribution along its core-to-rim profile. An approximately two-third part of the profile (from core-to-rim, marked on Fig. 5a), the concentration of Fe reaches its maxima (Alm 91.7%) and the concentrations of Ca and

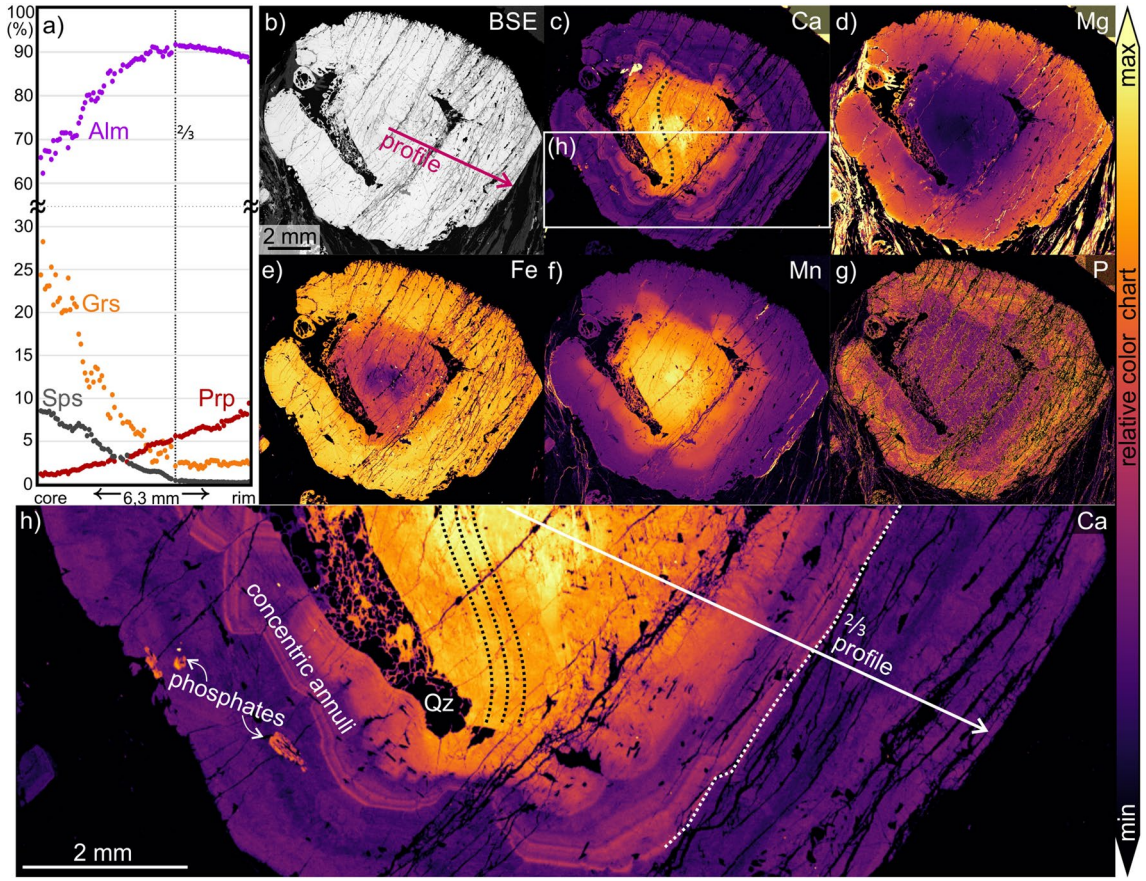

Fig. 5 **a** Compositional profile, **b** BSE image, and **c–h** compositional maps of a large porphyroblast of garnet (sample JK22-20); measured by WDS on EPMA; Ca- and Mn-maps are shown in relative logarithmic scale; in the P-map (**g**), a mask was applied to suppress elevated P concentrations within garnet fractures, represented in black color

Mn drop significantly (Grs 2.5; Sps 0.4%) but do not change markedly in the last one-third of the grain. The Mg content steadily increases rimward, reaching Prp 5.6% at the two-thirds point of the grain and a maximum (Prp 9.4%) at the very edge of the grain. A small decrease in Fe is apparent from its peak toward the edge of the grain (Alm 87.8%). The central part of the grain records a sigmoidal-oriented pattern of elevated Ca concentration, as marked by dotted lines on the Ca-map (Fig. 5c, h). A weak sigmoidal pattern of Mg and Fe can be also seen in the central part (Fig. 5d and e). This corresponds with the orientation of the chloritoid needle inclusions and their positions together with the inclusion positions of zircon and ilmenite (Fig. 3e–h). Closer to the rim from the central part of the grain, concentric annular (ring-shaped) zoning of Ca forms, with common thin annuli of slightly variating, short-wavelength element content. A local enrichment of P is evident in a concentric annular manner at the rim part of the grain (Fig. 5g). Well-developed major element zoning of garnet can be seen growing as well within an enclosed quartz band (Fig. 5h), resulting in a net-like texture between garnet and quartz.

Based on EPMA compositional mapping, three types of compositional zoning could be observed, as follows. The first type, (1) continuous change, is characterized by the continuous increase or decrease of element from the core towards the rim, typical for the major elements (Fig. 5c–f). The second type, (2) concentric annuli, is marked by concentric zoning with thin annular rings of increments or decrements of elements—short-wavelength fluctuations, as shown for the rim part of grain on the map of Ca and P (Fig. 5g, h). The third type, (3) overprint zoning, is characterized by sigmoidal-shaped bands of increments or decrements of elements that follow the spatial distribution and orientation of inclusions in the garnet. This third pattern type is most observable from the Ca-map, though only in the central part of grain (Fig. 5c, h). All three compositional zoning types are regularly found in combination, transitioning into each other in individual element maps.

Detailed LA-ICP-MS trace element mapping of garnet (Fig. 6) reveals a well-developed compositional zoning for several elements including Li, Na, Sc, Ti, V, Cr, Co, Zn, Y, Zr, Nb, and most of REE (HREE, MREE, Eu, Sm and

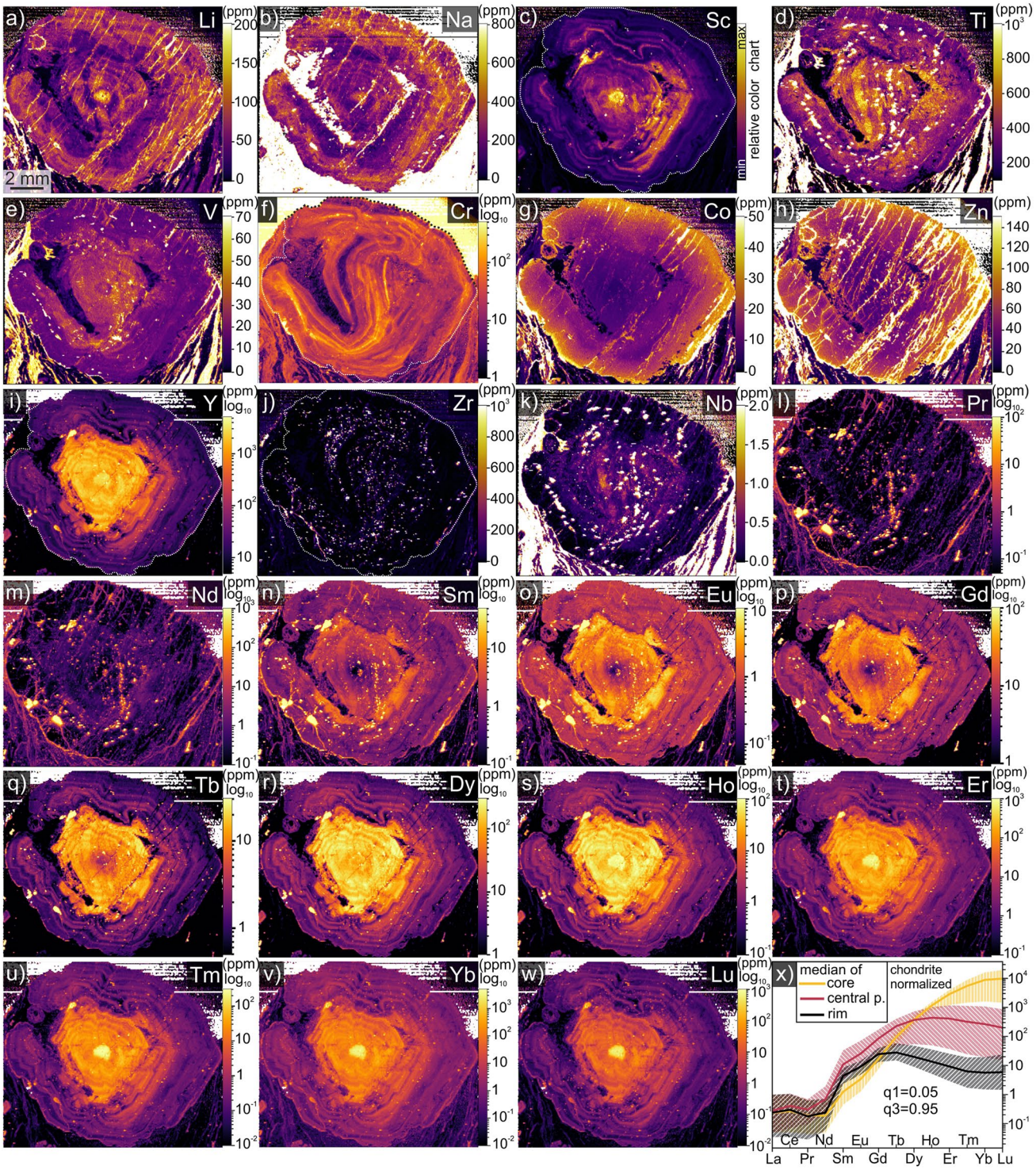

Fig. 6 Trace element maps featuring a large garnet grain and surrounding matrix minerals (quartz, phengite, biotite, and chlorite) from sample JK22-20, measured by LA-ICP-MS. Maps are sorted by increasing nucleon number of analyzed isotopes **(a–w)**. The maps are quantified, except Sc **(c)**, because of the peak overlay with Si analyzed values. Areal REE data of the core (highest values of HREE in center), central, and rim parts are plotted and normalized to the chondrite values according to Boynton (1984), while the medians are plotted as lines, and the range of values from q1 = 0.05 to q3 = 0.95 are shown as hatched transparent fields **(x)**

slightly also Nd and Pr). Three defined types of compositional zoning are well recognizable among them. The trace element maps of Ga, Rb, Sr, La, and Ce, which had no clear compositional zoning, are presented in the Supplementary Fig. 2S.

The first zoning type (continuous change) is well apparent on the maps of Co and Zn (Fig. 6g, h), where the element content continuously increases from the core toward the rim (Co ~ 5 → 35; Zn ~ 20 → 100 ppm), directly proportional to the distribution of Mg and inversely to that of Mn (Fig. 5d, f). Fractures in the garnet grain are commonly filled by chlorite and show abundant contents of Zn and partly also Co.

The second type (concentric annular changes) is visible in concentration maps of Li, Na, P, Sc, Ti, V, Y, and most of REE (Figs. 5g, 6a–e, i, n–w). These short-wavelength fluctuations of element content may be developed across whole grain from core to rim (Li, Na, Sc, V, Y, MREE, HREE; Fig. 6) or form visible annuli zoning only in the rim part of the grain (P, Ti, Sm, Eu; Figs. 5g, 6). Common distributional feature occurring in relation to this type of zoning is a notable enrichment by some elements in the core of the grain (Li ~ 160; Na ~ 450; Sc relative abundance; Y ~ 2 600; Ho ~ 90; Er ~ 750, Tm ~ 270, Yb ~ 3 200, and Lu ~ 560 ppm; Fig. 6a–c, i, s–w). The V and Dy contents show a fluctuating concentration in the core (Fig. 6e, r), and additionally, contents of Nd, Sm, Eu, Gd, and Tb are notably low in the core (Fig. 6m–q). Concentric annuli zoning of some elements shows good correlation in the central part of the grain, which is well visible from Li, Na, Sc, Y, MREE, and HREE, and slightly Eu, and Sm maps (Fig. 6a–c, e, i, o–w). The elements Sc, Sm, Eu, and Gd exhibit also non-uniform enrichment within the mantle part (i.e., the region dividing the central and rim part) of the grain. Higher concentrations of Nb and Nd are discernible in the central part of the grain, displaying a slightly higher concentric annular pattern (Fig. 6k, m). The compositional drop observable between the central part of grain and the rim is clearly visible for Y, HREE, MREE, Eu, and Sm (Fig. 6i, l–w). The REE contents at the rim are markedly lower, albeit with concentric annular variations evident in the element maps. Positions of the annuli correlate well among the maps of Sc, Y, and REE and on the rim part also with Li, Na, P, and Ti (Fig. 6a–d, i, n–w). The rim part of the grain exhibits also elevated concentrations of P, Li, and Na, with correlating annular changes (Figs. 5g, 6a, b), but anti-correlating the Ca distribution (Fig. 5c, h). The V content shows a sharp decrease followed by an increase in the core of grain, and the garnet is generally enriched by V in its central part (Fig. 6e). Comparatively insipid annuli of V contents are observed throughout the entire grain and exhibit positional alignment with the annular distribution of Sc, with which it shows a compositional anti-correlation.

The distribution of LREE within garnet exhibits a decreasing trend toward the lighter elements. Specifically, the map of Pr already reveals predominantly low abundance levels, besides areas corresponding to certain inclusions and fractures (Fig. 6l). The decrease in HREE values from the core to the rim and the trend of decreasing element abundance toward lighter elements (except for MREE enrichment outside the grain core) are well evident from the normalized values to chondrite (Fig. 6x). The central part of the grain is well-distinguishable from the rim part by the Y content being higher than 100 ppm. Content of Y at the central part decreases from 2 700 to 120 ppm, but at the rim part, it varies between 10 and 90 ppm across the concentric annuli (Fig. 6i).

The third zoning type (overprint distribution) shows a sigmoidal shape, tracks the spatial distribution of inclusions, and is particularly visible on the compositional map of Cr (Fig. 6f). On the map, it can be seen that high-Cr strings (~ 120 ppm) alternate with very low-Cr domains (3–20 ppm). Similar contents are visible in the matrix micas. Most of the high-Cr strings are parallel to the spatial distribution of ilmenite inclusions in garnet, which are particularly visible (white inclusions) on the map of Ti or Nb (Fig. 6d, k). Both Ti and Nb show abundant contents with a sigmoidal overprint distribution in the central part of the grain. High concentrations of Ti and Nb are observable in string-like formations, positionally corresponding to the low-Cr domains, and in part, to reduced amounts of Li (Fig. 6a, f). Zircon inclusions follow a sigmoidal pattern across the grain in the Zr-map, with no occurrence in areas of the lowest Cr content (see Fig. 6f, j). Some of these low-Cr areas correspond to a higher amount of enclosed quartz.

Sample F16-07 (Domašín)

Sample F16-07 exhibits garnet mainly with atoll texture, but with sporadic larger porphyroblasts of non-atoll garnet. The objectives for this sample encompass two aspects: first, to characterize the compositional zoning within a single grain (larger porphyroblast); and second, to compare the compositional variations among multiple garnet grains as well as other minerals present in the sample, which might help to understand the atoll texture formation. Within a single garnet porphyroblast, the compositional profiles and maps of the major and trace elements help to distinguish two garnets parts (Grt I and Grt II; Fig. 7), in the same manner as for the atoll garnets of sample JK2-19 (Fig. 4), but the compositional zoning with bell-shaped Ca and Mn distribution is closer to the garnet of sample JK22-20 (Fig. 5). In sample F16-07, the transition from Grt I into Grt II is characterized by sharp drop of Ca and peak Fe contents (Fig. 7a). Grt I is restricted to the central part of grain and is surrounded by Grt II on the rims. Grt II can occur as well in the central part, commonly in association with quartz in restricted domains (shown on Fig. 7b). Inside the atolls, Grt II can also create

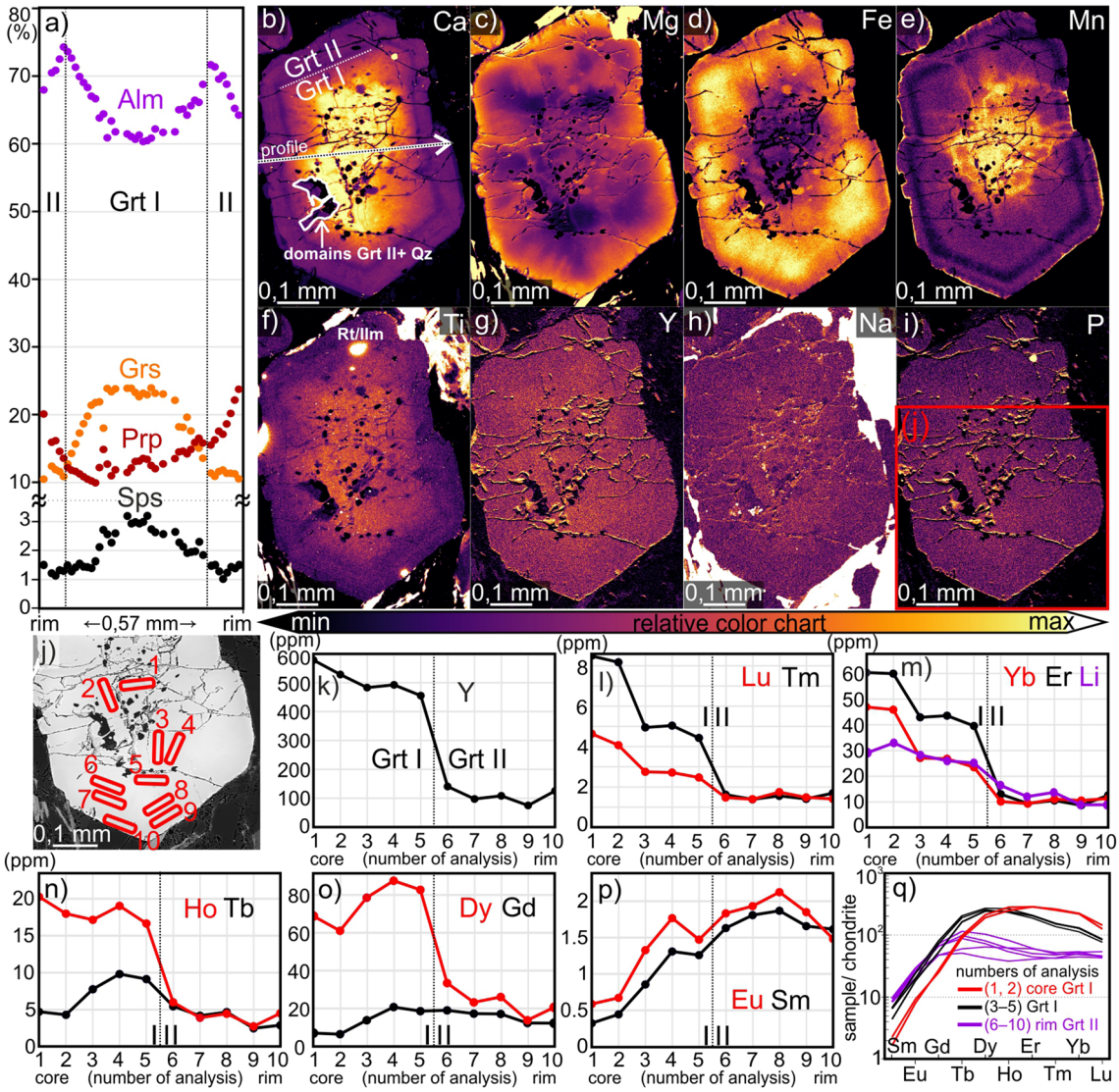

Fig. 7 **a** Compositional rim-to-rim garnet profile of main elements, recounted to the garnet endmembers (sample F16-07, measured by WDS on EPMA); **b–i** compositional maps of garnet main and trace elements (measured by WDS on EPMA); **j** BSE image of the garnet with marked positions of transects of conducted analyses; **k–p** compositional core-to-rim profile of trace elements (Li, Y, and REE) in the garnet (measured by LA-ICP-MS); **q** core-to-rim profile REE analyses normalized to the chondrite values of Boynton (1984)

islands and peninsulas surrounded by lagoons of matrix minerals. The atolls show consistent formation by Grt II, but possible Grt I can be present along the inner edges (Fig. 8a). The maps additionally depict a change in composition along nets that likely correspond to former microfractures within Grt I, which have been subsequently healed by garnet. These healed fractures exhibit higher Mg and Mn concentrations than the host garnet (Fig. 7c, e). The garnet exhibits growth zoning from the core to the rim, where Ca and Mn contents decrease from the core toward the Grt I/II transition, resembling a bell-shaped distribution (Grs 23.9 → 10.9; Sps 3.2 → 1.3%) with sharp drop of Ca close to the transition (Fig. 7a, b, e). Contents of Ca and Mn slightly fluctuate at the rims (Grs 10.9–11.9; Sps 1.0–1.5%), forming concentric annuli. The content of Mg increases continuously from the core toward the rim (Prp 10 → 23.8%), while Fe increases to its peak values at the Grt I/II transition (Alm 60.3 → 73.5%) and then decreases toward the rim (Alm 64.2%; Fig. 7a). Elevated contents of Ti, Y, Na, and P (very slight) in Grt I are visible from the compositional maps of trace elements (Fig. 7f–i).

Quantitative LA-ICP-MS measurements of Li, Y, and REE (only Eu and Sm from LREE, the rest of LREE was under the detection limit) were carried out in carefully selected spots/transects in garnet (ten analysis spots) to reflect core-to-rim profile development and to avoid fractures

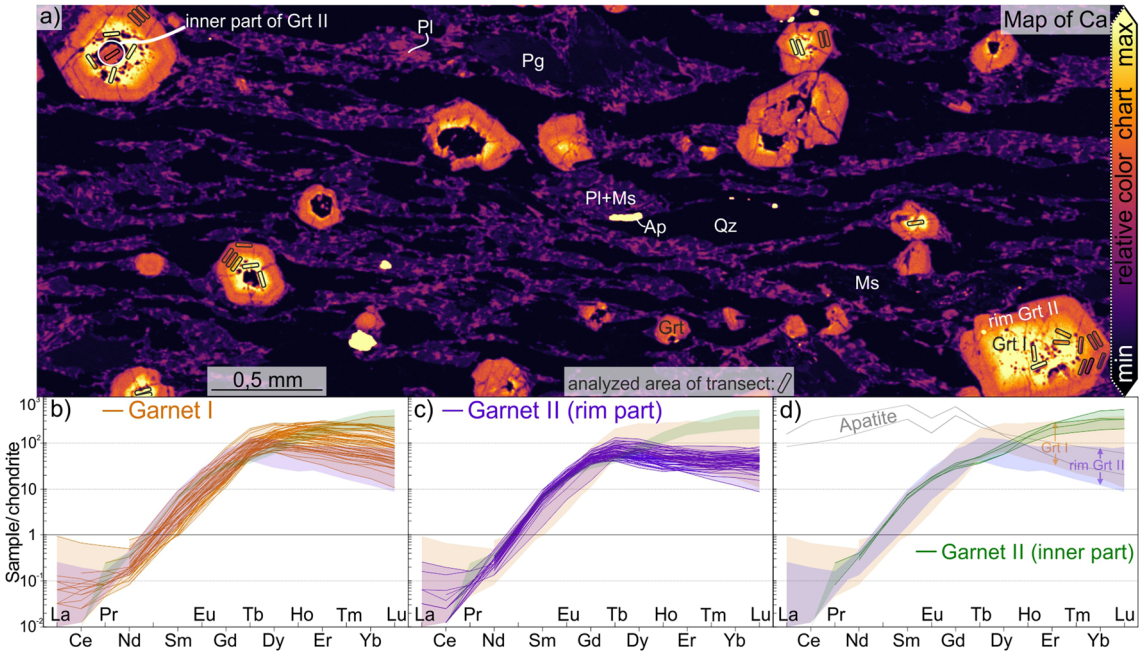

Fig. 8 Multiple garnet trace elements measurements from sample F16-07; **a** reduced section of a large (~10×10 mm) Ca-map with marked positions of analyzed transects in garnet grains (measured by WDS on EPMA), central Grt I showing abundance of Ca (yellow garnet parts) against Grt II on the rims or in the inner part as an island/peninsula (orange to magenta garnet parts); **b–d)** REE values of central Grt I **(b)**, rim Grt II **(c)** and inner Grt II + two apatite analysis **(d)**, measured by LA-ICP-MS and normalized to the chondrite of Boynton (1984)

and inclusions (Fig. 7j). The core of the garnet (spot n. 1, 2) is significantly enriched in HREE and shows the highest peaks of Y, Li, and Ho (Fig. 7k–n, q). The HREE contents then drop and Li with Y decreases less dramatically toward the Grt I/II transition. The Grt I is enriched by Ho and Dy of MREE and less by lighter REE, but their collective content increases toward the Grt I/II transition (Fig. 7n–q). The Li, Y, HREE, and Ho, Dy, and Tb of MREE drop markedly with the transition to rim Grt II and slightly fluctuate toward the very rim of the grain (Fig. 7k–o, q). The Gd concentration remains steady after the Grt I/II transition and decreases slightly at the very rim (Fig. 7o). The Eu and Sm of LREE shows steady increase up to their peak values after the Grt I/II transition and then decreases moderately toward the very rim (Fig. 7p).

To quantify and compare the overall Li + Y + REE budget of Grt I and Grt II in the rock while minimizing the effect of different grain sizes and cut positions through them, a total of 31 garnet grains of various sizes were analyzed (59 analyses in Grt I and 63 in Grt II, listed in Table 1S). Sample F16-07 was particularly suitable for this comparison due to the presence of a large number of relatively small garnets visible in its thin section. To analyze the trace element composition, the laser ablation was performed in the form of short transects at carefully selected positions in garnet grains, based on relatively large-scale compositional maps (~10×10 mm) of major elements (Fig. 8a), allowing to distinguish Grt I and II and their zoning. The resulted REE contents from garnets were then normalized to REE values of chondrite (Boynton 1984). The results show high abundance of HREE and MREE with decreasing trends toward the lighter REE (Fig. 8b–d). The central Grt I shows a wider range of higher HREE + MREE in the very core of the grain and lower concentrations closer to the Grt I/II transition (Fig. 8b). The rim Grt II shows a narrower range of values, overlapping mostly with the lower concentrations of HREE + MREE in Grt I, and shows generally higher values of LREE than in Grt I (Fig. 8c). The highest concentrations of HREE are observed within the inner Grt II (islands and peninsulas) situated inside the garnet atolls. These concentrations are comparable to, or greater than, the highest values detected within the Grt I (Fig. 8d). The distribution pattern of Y and Li mirrors that of the HREE concentrations (see supplementary Table 1S).

Compositional changes in other mineral phases

White mica is mainly represented by phengite, exhibiting variable Si content that is typically greater in the grain cores (JK2-19: 3.46; JK22-20: 3.54; F16-07: 3.48 a.p.f.u.), as shown in Fig. 9 and Table 2. Additionally, sample F16-07 includes muscovite with higher Na content

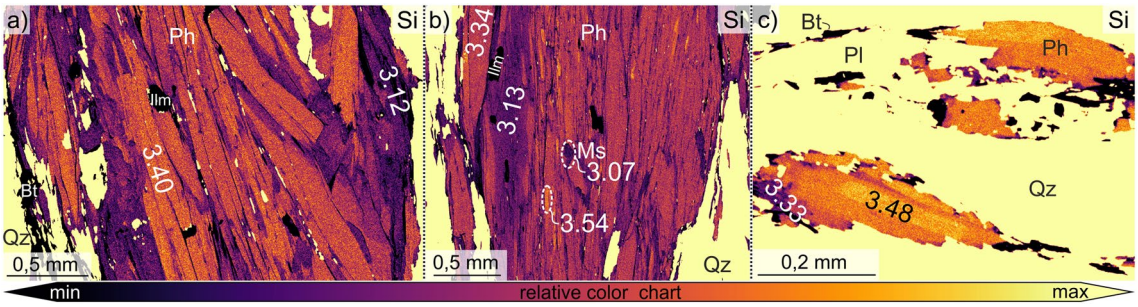

Fig. 9 Compositional maps of Si distribution in phengite grains with marked quantitative Si contents (in a.p.f.u.) from samples **a** JK2-19; **b** JK22-20; and **c** F16-07, measured by WDS on EPMA

(0.23 a.p.f.u.) and paragonite exhibiting low K content (0.08 a.p.f.u.). White micas have a high concentration of Li (Ms/Ph up to 210 ppm; Pg up to 170 ppm), Rb (Ms/Ph up to 350 ppm; Pg up to 10 ppm), and Sr (Ms/Ph up to 700 ppm; Pg up to 3000 ppm). Measured contents of Y, La, and Ce in white micas were close or under the detection limit. High concentrations of Ti, V, Cr, Zn, Ga, and Nb in phengite are apparent from the compositional maps (Fig. 6, Ga in supplementary Fig. 2S). The X_{Mg} ratios of chloritoid inclusions in garnet are increasing based on their position in garnet from core-to-rim part (0.05 → 0.10).

Among the minor and accessory phases, chlorite (~ 510 ppm) and staurolite (~ 3010 ppm) are notable for containing a substantial amount of Li, with lesser amounts detected in apatite (~ 6 ppm). Staurolite exhibits a high Zn content (0.06 a.p.f.u.). Although chlorite has only small amounts of Rb (< 2 ppm) and Sr (< 1 ppm), it has elevated concentrations of Co and Zn (Fig. 6g, h). Apatite displays a high concentration of Sr (up to 930 ppm), Y (up to 260 ppm), and REE, as depicted in Fig. 8d and outlined in Table 2.

Discussion

Major and trace elements distribution in garnet

Garnet is generally composed of a wide variety of elements and can undergo various heterovalent substitutions at all sites of its formula (Grew et al. 2013). The compositional changes/zoning of main and trace elements in metamorphic garnet can result from numerous simultaneous or subsequent factors (e.g., Lanzirotti 1995; George et al. 2018). Here we discuss the observed changes in garnet composition in studied HP micaschist samples to clarify possible processes of their formation and implications for the reconstruction of the host rock development and PT conditions.

Major changes in the major elements

The bell-shaped core-to-rim decrease of Mn in the central part of the grain appears to follow a Rayleigh distribution (Hollister 1966). However, concerning Ca, besides the bell-shaped distribution observed in garnets of samples JK22-20 and F16-07 (Figs. 5, 7), a plateau-like distribution in the central part of the garnet in sample JK2-19 (Fig. 4) is also evident. This, in combination with the findings of other Ca-bearing matrix phases, indicates a stronger control by broad core-to-rim partitioning along the P–T path rather than Rayleigh fractionation. The prograde major element distribution, mainly steady core-to-rim increase of X_{Mg}, is in agreement with previous studies reconstructing HP peak conditions of garnet micaschists from the area of central Erzgebirge (Konopásek 2001; Jouvent et al. 2022).

The compositional jump (or steep bell-shaped change) between Ca-rich central Grt I and Ca-poor rim Grt II can be explained by (1) formation of two generations of garnet, where compositionally distinct parts reflect conditions of growth during different metamorphic events (e.g., Faryad et al. 2019, 2022b); or (2) a discontinuous garnet growth during one prograde path, where the central and rim parts grow at lower and higher grade conditions, respectively (Vance and O'Nions 1990; Dachs and Proyer 2002; Konrad-Schmolke et al. 2006, 2008a; Kulhánek et al. 2021). The transition between two compositionally different garnet parts might be also partly or fully equilibrated by intracrystalline diffusion, especially in case of major divalent elements (Dachs and Proyer 2002; Faryad and Ježek 2019; Faryad et al. 2022a). Considering that the second case has been described for garnets in neighboring metabasites (Kulhánek et al. 2021) and the prograde path of garnet growth has been assumed for other micashists from the studied area (Konopásek 1998; Jouvent et al. 2022), it is, therefore, also favored for the compositional development of garnets from metapelites of this study.

Table 2 Chemical analyses of studied minerals; oxides measured by WDS on EPMA and expressed in weight percent and calculated on cations of crystal chemical formulas and X_{Mg}; trace elements measured by LA-ICP-MS (Li, Rb, Sr, Y, and REE) and expressed in ppm; blank area—element not measured; < DL—under detection limit; approximate data (~) extracted from several measured points of the compositional LA-ICP-MS maps

Sample:	JK2-19	JK22-20	JK2-19	JK22-20	F16-07	F16-07	F16-07	F16-07	F16-07	F16-07	F16-07	F16-07
Mineral:	Zo/Ep	Cld	Ph	Ph	Ph	Ms	Pg	Bt	Chl	Pl	St	Ap
Position:	Matrix	Incl	Matrix	Matrix	Matrix	Matrix	Matrix	Matrix	Matrix	Matrix	Matrix	Matrix
SiO_2	38.53	24.02	51.44	49.37	52.01	44.04	45.39	35.13	26.93	63.25	27.30	< DL
TiO_2	0.27	< DL	0.28	0.26	0.21	< DL	< DL	1.49	< DL	< DL	0.33	< DL
Al_2O_3	26.50	39.04	26.24	29.03	26.89	36.54	38.77	18.85	19.35	21.78	54.74	< DL
FeO_{tot}	8.31	26.33	3.03	2.82	2.10	0.75	0.30	16.57	27.22	< DL	11.15	< DL
MnO	0.15	0.21	< DL	< DL	< DL	< DL	< DL	< DL	0.18	< DL	0.14	< DL
MgO	0.077	0.93	3.25	2.31	3.86	0.26	0.074	11.52	12.29	< DL	1.53	< DL
ZnO	< DL	< DL	< DL	< DL	< DL	< DL	< DL	< DL	< DL	< DL	0.55	< DL
CaO	22.78	0.038	< DL	< DL	0.006	< DL	< DL	< DL	0.11	2.97	< DL	55.99
BaO	< DL	< DL	< DL	< DL	< DL	1.28	< DL	< DL	< DL	< DL	< DL	< DL
Na_2O	< DL	< DL	0.47	0.54	0.46	2.14	6.76	0.072	< DL	9.68	< DL	< DL
K_2O	0.10	< DL	9.28	9.98	7.38	7.87	1.00	8.94	< DL	0.064	< DL	< DL
P_2O_5	0.059	< DL	< DL	< DL	< DL	< DL	< DL	< DL	< DL	< DL	< DL	43.99
Total	96.79	90.57	93.98	94.31	92.92	92.89	92.29	92.57	86.07	97.75	95.73	99.98
O	12.5	6	11	11	11	11	11	11	28	8	24	12.5
Si	3.04	1.02	3.46	3.33	3.48	3.00	2.99	2.71	5.83	2.85	4.00	< DL
Ti	0.016	< DL	0.014	0.013	0.011	< DL	< DL	0.086	< DL	< DL	0.036	< DL
Al	2.46	1.96	2.08	2.31	2.12	2.94	3.01	1.71	4.93	1.16	9.44	< DL
Fe^{3+}	0.49	< DL	< DL	< DL	< DL	< DL	< DL	< DL	< DL	< DL	< DL	< DL
Fe^{2+}	< DL	0.94	0.17	0.16	0.12	0.043	0.016	1.07	4.92	< DL	1.36	< DL
Mn	0.0099	0.0075	< DL	< DL	< DL	< DL	< DL	< DL	0.032	< DL	0.017	< DL
Mg	0.0091	0.059	0.33	0.23	0.38	0.027	0.0072	1.32	3.96	< DL	0.33	< DL
Zn	< DL	< DL	< DL	< DL	< DL	< DL	< DL	< DL	< DL	< DL	0.059	< DL
Ca	1.92	0.0017	< DL	< DL	0.0004	< DL	< DL	< DL	0.026	0.14	< DL	4.90
Ba	< DL	< DL	< DL	< DL	< DL	0.034	< DL	< DL	< DL	< DL	< DL	< DL
Na	< DL	< DL	0.061	0.070	0.059	0.28	0.86	0.011	< DL	0.85	< DL	< DL
K	0.010	< DL	0.80	0.86	0.63	0.68	0.084	0.88	< DL	0.0037	< DL	< DL
P	0.0039	< DL	< DL	< DL	< DL	< DL	< DL	< DL	< DL	< DL	< DL	3.04
Total	7.97	3.99	6.91	6.97	6.80	7.01	6.98	7.79	19.71	5.00	15.25	7.94
X_{Mg}	1.00	0.06	0.66	0.59	0.77	0.38	0.31	0.55	0.45	–	0.20	–
Li				~50	202.0	209.6	169.7		508.7	< DL	3010.1	5.57
Rb				~450	343.3	332.96	8.76		1.55	< DL	< DL	< DL
Sr				~40	628.8	691.1	2964.1		0.72	< DL	< DL	925.1
Y				~0.04	< DL	0.11	< DL		< DL	< DL	< DL	255.7
La				~0.02	0.05	0.06	0.03		< DL	< DL	< DL	25.85
Ce				~0.04	0.02	0.06	0.03		< DL	< DL	< DL	79.90
Pr				< DL	< DL	< DL	< DL		< DL	< DL	< DL	14.59
Nd				~0.02	< DL	< DL	< DL		< DL	< DL	< DL	99.08
Sm				< DL	< DL	< DL	< DL		< DL	< DL	< DL	63.99
Eu				~0.02	< DL	< DL	< DL		< DL	< DL	< DL	12.06
Gd				< DL	< DL	< DL	< DL		< DL	< DL	< DL	102.0
Tb				< DL	< DL	< DL	< DL		< DL	< DL	< DL	10.65
Dy				< DL	< DL	< DL	< DL		< DL	< DL	< DL	50.75
Ho				< DL	< DL	< DL	< DL		< DL	< DL	< DL	9.06
Er				< DL	< DL	< DL	< DL		< DL	< DL	< DL	21.53
Tm				< DL	< DL	< DL	< DL		< DL	< DL	< DL	2.78

Table 2 (continued)

Sample:	JK2-19	JK22-20	JK2-19	JK22-20	F16-07	F16-07	F16-07	F16-07	F16-07	F16-07	F16-07	F16-07
Mineral:	Zo/Ep	Cld	Ph	Ph	Ph	Ms	Pg	Bt	Chl	Pl	St	Ap
Position:	Matrix	Incl	Matrix	Matrix	Matrix	Matrix	Matrix	Matrix	Matrix	Matrix	Matrix	Matrix
Yb				< DL	< DL	< DL	< DL		< DL	< DL	< DL	14.99
Lu				< DL	< DL	< DL	< DL		< DL	< DL	< DL	1.93

Core-to-rim continuous increase of Co and Zn

The distribution of Co and Zn corresponds with the spatial distribution of Mg and is inversely related to Mn. This can be attributed to the substitution of Co and Zn at the dodecahedral (X) site of garnet formula, which is supported by the similar ionic radii of divalent Co^{2+} and Zn^{2+} in the eightfold coordination number (^{VIII}) with the major elements of garnet, particularly Fe^{2+}, Mg^{2+}, and Mn^{2+}. Among the possible sources of Zn and Co incorporated into garnet are the dissolution of prograde chlorite, and even more so, biotite, which are enriched in these elements (Fig. 6g, h; George et al. 2018). The partitioning of Co and Zn between garnet and biotite, which is the possible main source, has been reported in equilibrium, with the distribution of these elements as a function of temperature (Yang et al. 1999), that is, noticeably similar but with inverse temperature dependence as Mn.

Concentric annular zoning

Concentric annular zoning is characterized by the formation of usually thin annuli, that is, ring-shaped zones of increase or decrease of a certain element in the crystal. Similar zonation in metamorphic garnet is thought to be formed by several possible processes, namely (1) the incorporation of main and trace elements from main phases undergoing the garnet-forming reaction (Konrad-Schmolke et al. 2008b); (2) partitioning into garnet from the breakdown of trace elements' rich accessory phases (e.g., Pyle and Spear 1999; Yang and Rivers 2002; Yang and Pattison 2006; Raimondo et al. 2017; Rubatto et al. 2020; Gaidies et al. 2021); (3) diffusion-limited uptake from the matrix, in which local peaks of element concentrations reflect thermally activated diffusion due to temperature increase (Skora et al. 2006); (4) varying growth rates of garnet and the incorporation of pre-existing heterogeneities with variable major and trace element concentrations from the matrix (George et al. 2018); (5) infiltration of an externally derived fluid carrying element concentrations which are out of equilibrium with mineral phases of the infiltrated rock (Jamtveit et al. 1993; Dziggel et al. 2009; Moore et al. 2013); (6) recurrent changes in the transport permeability of rock elements associated with changing fluid fluxes through the host rock during garnet growth (Konrad-Schmolke et al. 2023); and finally, (7) dissolution and reprecipitation of garnet, which can be subdivided into (7a) the dissolution of compositionally zoned garnet from its core through microfractures and incorporation of elements into concurrently growing garnet on the rim during one prograde path (Kulhánek et al. 2021); (7b) the partial resorption of garnet and release of elements into the matrix during retrogression of the rock and back-incorporation of elements during the second garnet-forming metamorphic event (Jedlicka et al. 2015); and (7c) recurrent release and the incorporation of elements during fluctuating garnet stability (growth/resorption process) as a response to pressure pulses reflecting seismic cycles during subduction (Viete et al. 2018). The formation of annuli zoning in our samples was interpreted to result from a combination of at least four of these processes (1, 2, 6, and 7a), as discussed in more detail below.

Linkage of Y + REE annuli with other trace elements. The trivalent cations of Y + REE substitute the divalent major elements (M = Mg, Fe, Mn, or Ca) with similar ion size on the dodecahedral (X) site of the garnet structure. To maintain electroneutrality, there must be compensation of the charge by coupling the substitution of Y + REE with other elements or possibly vacancies (Carlson et al. 2014). The low diffusion coefficients of Y + REE against M produces a highly resistant record of compositional changes during garnet growth, as has been shown by the zonal distribution of the Y + REE and their co-substituents in garnet (Tirone et al. 2005; Carlson 2012; Cahalan et al. 2014).

Among the commonly described substitution schemes, the alkali- ($^{VIII}Y^{3+} + {}^{VIII}[Na^{+}, Li^{+}] = 2\ {}^{VIII}M^{2+}$) and menzerite-like ($^{VIII}Y^{3+} + {}^{VI}[Mg^{2+}, Fe^{2+}] = {}^{VIII}M^{2+} + {}^{VI}Al^{3+}$) substitutions of Y(+REE) in garnet were calculated by Carlson et al. (2014) and deemed to represent more energetically favorable options than the YAG- ($^{VIII}Y^{3+} + {}^{IV}Al^{3+} = {}^{VIII}M^{2+} + {}^{IV}Si^{4+}$) or vacancy-like ($^{VIII}Y^{3+} + {}^{VIII}\square = 3\ {}^{VIII}M^{2+}$) coupled substitutions. The alkali-coupled substitution corresponds well with our observation of positionally agreeing core and annuli enrichments of Y + HREE + MREE with Na and Li (Figs. 4, 6, 7), and is commonly observed among HP rocks (George et al. 2018; Bebout et al. 2022). Upon comparing the elemental abundances in the garnet (in a.p.f.u.), a strong correlation between the Y and the combined amounts of Li + Na is evident in the central part of the

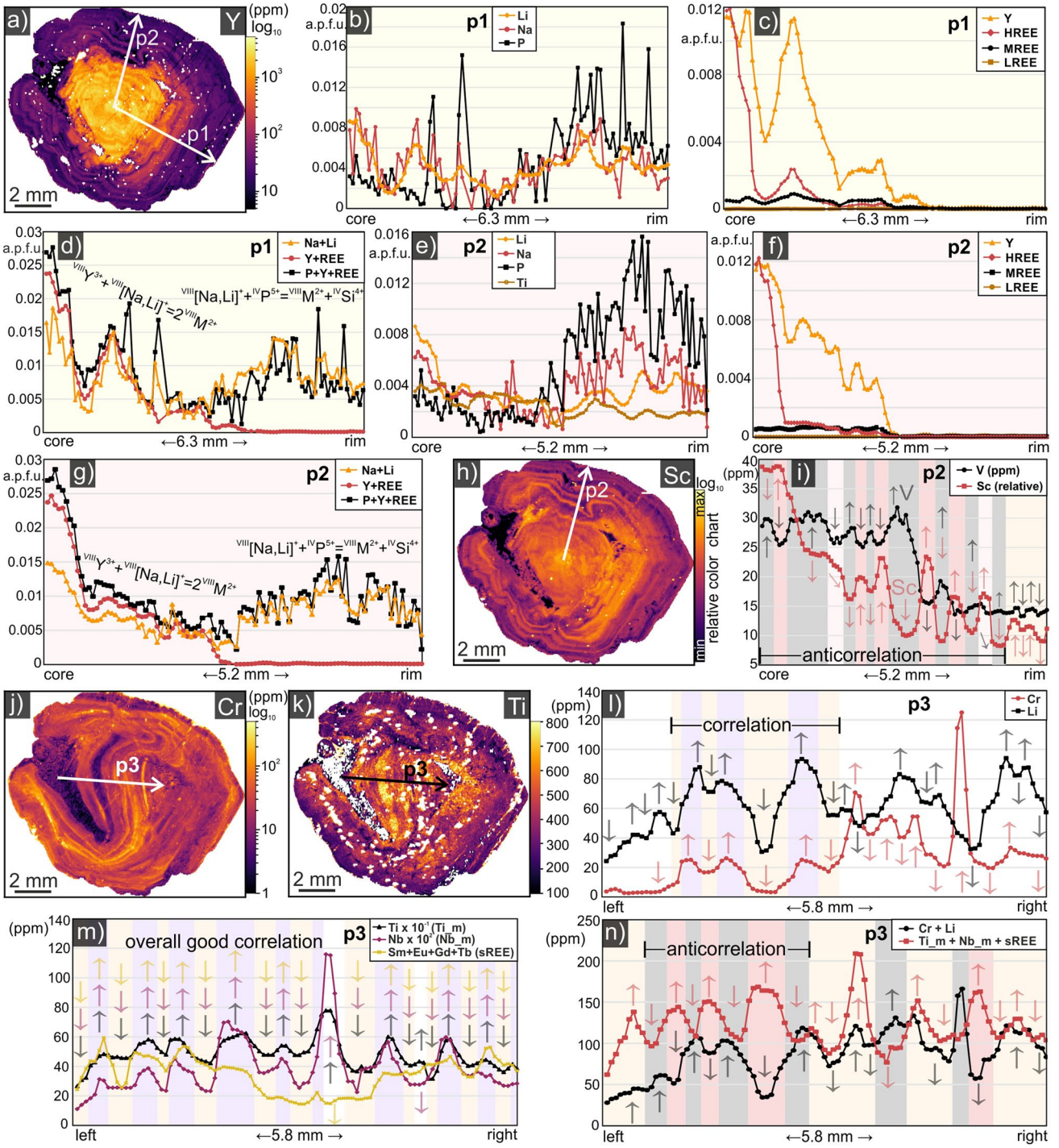

Fig. 10 Trace element profiles in garnet of sample JK22-20; **a** Y-map with garnet mask setting and marked two profiles; **b–g** composition profiles 1 and 2 with Li, Na, P, Y, and REE contents displayed; the coupled Y-alkali and P-alkali substitutions are displayed in a.p.f.u.; **h** Sc-map with garnet mask setting and marked profile 2; **i** V and Sc profile showing anti-correlating V/Sc oscillations, V in ppm and Sc relative; **j–k** Cr- and Ti-map with garnet mask setting and the marked third profile in the central part of garnet; **l–n** composition profile 3 with Li, Ti, Cr, Nb, Sm, Eu, Gd, and Tb contents displayed in ppm, selected REE are displayed together as a sum (sREE) and Ti and Nb are rescaled to better correlate changes with other elements: $Ti\_m = Ti \times 10^{-1}$, $Nb = Nb \times 10^{2}$; note that the Cr + Li anti-correlates with other elements in left part of the profile

garnet of sample JK22-20 (Fig. 10a–g). However, if we also include REE, (mainly HREE), which are significantly elevated in the very core of the grain, the abundance of Li + Na is no longer sufficient for coupled substitution with REE (Fig. 10d, g), and therefore we might expect a menzerite-like substitution for REE. The Li + Na content in the central part can be noticeably locally elevated above the Y content, due to coupled substitution with P.

It has been proposed that trivalent Sc can substitute into garnet X-site due to its similar ionic radius with divalent M (Jaffe 1951; van Westrenen et al. 1999; Yang et al. 1999). Such a substitution has been described through coupled heterovalent exchange in pyrope as: $^{VIII}Sc^{3+} + {}^{IV}Sc^{3+} = {}^{VII-I}Mg^{2+} + {}^{IV}Si^{4+}$ (Oberti et al. 2006), but the atomistic simulations of van Westrenen et al. (2000) have also shown that the coupled substitution of Sc^{3+} with Li^{+} into the garnet X-site (similar to the Y-alkali-like substitution scheme) is an energetically possible configuration. The homovalent exchanges on the garnet Y-site ($^{VI}Sc^{3+} = {}^{VI}Al^{3+}$ or $^{VI}Sc^{3+} = {}^{VI}Fe^{3+}$) have been described in Ca-rich garnets, where Ca on the X-site provides relaxation of the averaged garnet structure (Oberti et al. 2006; Quartieri et al. 2006). From the main phases of metapelitic rock, a considerable content of Sc was found to originate from garnet and biotite, among which the distribution of Sc should be governed mainly by the occupation of tetrahedral sites of biotite by Al^{3+} or Sc^{3+} rather than being related to the thermal change (Yang et al. 1999). Based on the spatially consistent annular enrichment of Sc with Y and HREE in garnet, but with distinct patterns of elemental representation values, it can be inferred that the incorporation of the increased concentrations of Y + HREE and Sc occurred concurrently, albeit exhibiting divergent patterns of element uptake. Regarding the Sc substitution mechanism, we cannot rule out any of those mentioned because of the small Sc abundances which were measured, but we do know that Sc is increased at sites of Y increase, which may suggest possible coupled substitution with alkalis (Li, Na).

The V-rich central part of the garnet (Fig. 6e) may reflect the continuous decomposition of major mineral phases such as chlorite and micas, which carry sufficient trace amounts of V (Spandler et al. 2003; George et al. 2018), during early garnet growth. The observed gains and losses are positionally anti-correlating with Sc, except for the outermost part (Figs. 6c, e, 10h, i), perhaps suggesting competitive behavior of these elements for the garnet formula site. It has been described that trivalent V, similar to that of Sc, preferentially enters the Y-site of garnet, with Ca providing the relaxation of structure at the X-site (Bordage et al. 2010). This would rule out coupled substitution of Sc with alkali. As was reported from garnet mantle rocks, V is less compatible in the garnet structure under higher fO_2 conditions compared to Sc (Canil 2002; Righter et al. 2011); therefore, the observed Sc/V differences may be due to variations in the fO_2 of the rock matrix during garnet growth. Such fO_2 variations have been documented by the H_2O content of garnet, which reflects the release of fluids during dehydration reactions, such as chlorite breakdown (Zhu et al. 2022).

Linkage of Ca annuli with trace elements. The observed negative correlation between the Ca annuli present in the mantle and rim part of a large garnet grain from sample JK22-20 and the distribution of P, Li, and Na suggests that these elements may be part of one coupled substitution scheme. A similar pattern (without measuring Li) in the garnets from the studied area was observed by Jouvent et al. (2022), who suggested the formation of garnet rims enriched by Na and P during HP conditions based on comparisons with studies from different terrains (Schertl et al. 1991; Ye et al. 2000) and experimental works describing elevated Na and P contents as possible HP to UHP indicators (Thompson 1975; Brunet et al. 2006; Konzett and Frost 2009). This type of formation mechanism would be possible through the coupled substitution of $^{VIII}Na^{+} + {}^{IV}P^{5+} = {}^{VIII}(Mg, Ca)^{2+} + {}^{IV}Si^{4+}$ (Thompson 1975; Hermann and Spandler 2008) leading to an Na-phosphate $Na_3Al_2P_3O_{12}$ with garnet structure, as synthetized by Brunet et al. (2006). The coupled substitution of Li and P has been experimentally confirmed, as well as that of Na, in HP to UHP conditions in garnet in the form of $^{VIII}Li^{+} + {}^{IV}P^{5+} = {}^{VIII}Mg^{2+} + {}^{IV}Si^{4+}$ (Hanrahan et al. 2009a). Based on our observations, which indicate that Li distribution fits well with the P and Na annuli enrichments and Ca annuli decreases in the garnet mantle and rim (Figs. 5g, h, 6a, b), we speculate that the coupled substitution of $^{VIII}(Na, Li)^{+} + {}^{IV}P^{5+} = {}^{VIII}Ca^{2+} + {}^{IV}Si^{4+}$ may play dominant role for Na and Li incorporation in this part of the garnet. This can be clearly seen when comparing the amount of (Na + Li) and P in the a.p.f.u. in the rim part of the garnet, for which the Y + REE concentrations are minimal (Fig. 10a–g). This alkali + P substitution also takes place in the central part of garnet, but in the shadow of dominant alkali + Y + REE coupled substitution (Fig. 10a–g).

The decomposition of apatite in the matrix during garnet growth and the partitioning of P into garnet along with Na and Li to balance electroneutrality in the structure could be a possible source of the steep increase in these elements. This is suggested by the observation of apatite inclusions in the central part of the garnet grain (Figs. 3d, g; 5g), for which the P content of garnet is lower, and the observed replacement pattern may be apatite grains → florencite → monazite + xenotime + paragonite → allanite (Fig. 3d, i), all of which occur as inclusions in the rim part of garnet with higher P concentrations (Fig. 5g). This is further supported by the rare occurrences of pseudohexagonal pseudomorphs after apatite inclusions, in which we observed a remnant apatite in the core enveloped by florencite, along with monazite together with paragonite.

While the central part displays sigmoidal overprint zoning in Ti, here we discuss potential mechanism behind the formation of a faint annular zoning at the rim part that corresponds with the position of annular abundance of P, Li, Na, and Sc (best seen in the upper part of the grain, Figs. 5g; 6a–d; 10e). Elevated Ti, P, and Na abundances have also been found in HP to UHP garnets in granulites from Erzgebirge, but with Ti elevated in the central part and diffusively depleted at the rim during the retrograde path (Ague and Axler 2016). This supports the attainment of only mid-high temperatures in the studied garnets, allowing the oscillatory zoning of Ti to be preserved at the rim. In that case, Ti would favorably accommodate the octahedral site of garnet by coupled substitution with Na ($^{VIII}Na^{+} + {}^{VI}Ti^{4+} = {}^{VIII}M^{2+} + {}^{VI}Al^{3+}$) or with Al on the tetrahedral site ($^{VI}Ti^{4+} + {}^{IV}Al^{3+} = {}^{VI}Al^{3+} + {}^{IV}Si^{4+}$) (Ringwood and Major 1971; Hermann and Spandler 2008). In this study, we observe that almost all of the Na + Li at the grain rim is involved in coupled substitution with P. Based on this finding, we propose that Ti may dominantly be in coupled substitution with Al. The weak oscillatory zoning of Ti in the rim part of the grain (Fig. 10e) is likely attributed to the irregular release of Ti during ilmenite breakdown, as indicated by the presence of ilmenite inclusions in the central and mantle part and rutile inclusions in the rim part.

Ca and Mn annuli in atoll garnet. The annuli of Ca and Mn fluctuating concentrations on the rim of garnet from the sample F16-07 (Fig. 7b, e) may be resulted from the dissolution and recrystallization of garnet, as introduced in Kulhánek et al. (2021). This process is merely proposed, as the sample also apparently undergoes dissolution of Mn- and Ca-rich Grt I in the central part of the grain and simultaneous crystallization of Grt II at the rim, as further discussed below, in Subsect. "Atoll garnet formation".

Overprint zoning

Overprinting of an element distribution from the matrix phases consumed by the garnet grain is thought to occur when the temperature of the system is not sufficient to enhance the mobility of a given element that would otherwise uniformly distribute to the garnet rims and form a concentric increment. Such immobility of an element, typically Cr, in the intergranular medium of matrix phases during garnet growth, can be explained by the lack of local chemical equilibration along the garnet grain interface. The overprint zoning of Cr in garnet gradually transitions to concentric annuli zoning in garnet zones formed under HT conditions, which can be attributed to the increased Cr diffusivity and the decreased garnet growth rate (Yang and Rivers 2001; George et al. 2018). Yang and Rivers (2001) report the Cr-overprint zoning formation in garnet from amphibolite-facies conditions for metapelitic rock, and the beginning of Cr-annuli formation in garnet above 660 °C. The Cr easily enters the Y-site of garnet through homovalent substitution ($^{VI}Cr^{3+} = {}^{VI}Al^{3+}$). The sigmoidal shape across whole grain is observable by a Cr-enriched strings (Fig. 6f), accompanied by sigmoidal distribution of Cld, Ilm, Rt, and Zrn inclusions (Fig. 6d, k). The well-developed overprint of Cr distribution from the matrix phases into the entire garnet grain might suggest sub-HT conditions (~ up to 600–700 °C) in combination with not sufficiently low garnet growth rate. The constraint on the overprint distribution of Ca, Ti, Nb, Sm, Eu, and Gd, and to a certain extent, Tb, solely to the central part of the grain, can be attributed to the lower mobility of these elements during the growth of the central part of the garnet at LT–MT conditions (~ 450–500 °C, compared with PT modeling of Grt-bearing micaschists from the studied area by Jouvent et al. (2022).

Due to the low mobility of Cr, the high- and low-Cr areas or strings most likely follow the original distribution in matrix phases replaced by garnet. Among the probable sources, relatively higher Cr likely originates from ilmenite and rutile grains. Titanite, which was found only sporadically as an inclusion in the very core of garnet grains, generally has very low Cr contents but high Nb and REE contents in metamorphic rocks (Cave et al. 2015; Garber et al. 2017; Kohn 2017; Gaidies et al. 2021; Konrad-Schmolke et al. 2023). Rutile contains a higher Cr content (~ 180 to 270 ppm; Table 1S) than ilmenite (up to 70 ppm; Table 1S). The Cr is partly released into the overgrowing garnet and creates Cr-rich strings spatially overlapping with most of the ilmenite/rutile inclusions, as visible on the Ti-, Cr-, and Nb-maps (Fig. 6d, f, l). Another possible source of Cr could be micas, as seen in the Cr-map (Fig. 6f). This is consistent with other research that suggests chlorite may be a potential source, connecting former phyllosilicate-rich layers to Cr-rich domains within garnet, and former quartz layers to Cr-poor domains (Yang and Rivers 2001; George et al. 2018). This is supported by observations of entrapped and partly dissolved quartz layers in garnet where the lowest concentrations of Cr in garnet are found (Fig. 6f). Most of the rutile/ilmenite and zircon inclusions do not occur in low-Cr domains, reflecting the former dominant distribution of rutile/ilmenite and zircon in the phyllosilicate layer prior to garnet encasement. The lowest Cr contents in the core part correlate with the low-Li string and anti-correlate with high-Ti, Nb, Sm, Eu, Gd, and Tb, and partly also high-Ca, sigmoidal domains of assumed former quartz layers (Fig. 10j–n). This pattern can be explained by the presence of other phases carrying relatively high amounts of Ti, Nb, Sm, Eu, Gd, Tb, and Ca, but low amounts of Cr and Li, within the former garnet-replaced quartz layer, such as the aforementioned titanite. The HREE distribution is not elevated in this sigmoidal pattern due to blending into the background of already high HREE values in the central part of the grain. The low Cr content in these

domains is most likely caused by strong immobility of Cr, that is, overprinting of the low Cr content in the quartz layer. Similar to Cr, Li tends to enter the garnet structure less readily when it forms in the intergranular space of quartz grains, which is visible especially in central part of garnet grains (Figs. 6a; 10l, n).

The presence of overprint zoning might reflect the rotation of the garnet grain during its growth and progressive absorption of foliated matrix phases during rock shearing (e.g., Schoneveld 1977; Passchier et al. 1992), or it may reflect a non-rotating garnet with progressively overgrowth that developed foliation of the matrix phases, thereby reflecting the foliation changes as it encloses them during its growth (e.g., Bell 1985; Bell and Johnson 1989; Hickey and Bell 1999). In our sample, the garnet shows not only spiral zoning, but also a more complex sigmoidal pattern, which could have resulted either from the second case of the described overprinting, or a combination of both cases.

Garnet growth and dissolution implications from elements distribution

Non-atoll garnet growth

Garnet nucleation apparently began under MP/MT (~ 1.0–1.5 GPa and ~ 450–500 °C) conditions, as has been suggested for garnet-bearing micashists from this area (Jouvent et al. 2022) and from the PT path of adjacent eclogites (Kulhánek et al. 2021). The garnet core contains high numbers of Mn and Y + HREE, which are elements that preferentially enter the garnet structure among the main metamorphic phases and can stabilize the garnet growth (Hollister 1966; Otamendi et al. 2002; Skora et al. 2006; Likhanov 2019). The high abundances of Sc, Y, and HREE in the very core of the garnet grain, compared to the rest of the central part (Fig. 10a–g), might originate from a rapid diffusion-limited uptake of these elements from the matrix into the garnet after nucleation, rather than being explained by the Rayleigh fractionation alone. This early consumption of large quantities of these elements by garnet would result in the creation of "diffusion halo" around the early grain, as introduced by Skora et al. (2006) and reported by George et al. (2018). The concentrations of Sc, Y, and HREE in the subsequently grown surrounding part of the early garnet would be markedly reduced, as observed in the studied garnet (Figs. 6, 10).

The observed prograde zoning of major divalent elements in garnet, characterized by the decrease in Ca and Mn content and increase in X_{Mg} (Figs. 4, 5, 7), indicates a PT path growing up to HP–MT conditions (compared with PT modeling of Grt-bearing micashists from the area; Konopásek 2001; Jouvent et al. 2022). This is supported by PT-sensitive crystallization sequences observed as inclusions from the core to rim of garnet (Ttn-Ilm-Rt). Additionally, the observations of the distribution of some trace element zoning patterns may support such PT development. These include: (1) gradually increasing Co and Zn contents toward the rim, which behave similarly to Mg and anti-correlate Mn, indicating in particular a continuous increase in temperature; (2) overprint zoning of Ti and partly of Ca, Sm, Eu, Gd, and Tb in the central part, which changes to purely concentric annular zoning in the rim part that can potentially be explained by increasing diffusivity with temperature; (3) well-developed overprint zoning of Cr throughout the garnet grain, suggesting its effective immobility in sub-HT conditions (~ up to 600–700 °C with relatively slow garnet growth rate; Yang and Rivers 2001); and (4) depletion of Y + HREE + MREE in the rim part and enrichment of coupled $^{VIII}(Na, Li)^{+} + {}^{IV}P^{5+}$ substitution elements, which has been experimentally documented from HP to UHP conditions (slightly elevated Na + P identified under 1.8–4.5 GPa experiments in prepared mantle-rock garnet; Thompson 1975; other experiments show UHP conditions for such substitution designed on mantle conditions; Brunet et al. 2006; Hanrahan et al. 2009b; Konzett and Frost 2009). In atoll garnet rims, Y + HREE + MREE content can be elevated as a consequence of the atoll forming process, as discussed further in Subsect. "Atoll garnet formation".

The fact that the PT path of studied rocks achieved HP conditions is supported by several other observations, such as high Si a.p.f.u. in matrix phengites (up to 3.54), kyanite in the matrix, increasing X_{Mg} of chloritoid inclusions within the garnet from the core toward the rim (0.05 → 0.10) and its disappearance/decomposition during rim growth, and the Ti-bearing phase crystallization sequence, involving titanite (very core inclusion in Grt) → ilmenite (central and inner part of rim inclusion) → rutile (rim part inclusion).

The documented thin annular oscillations of the various elements (Li, Na, P, Ca, Sc, Ti, V, Y, and REE) in garnet of sample JK22-20 (Figs. 5, 6, 10) are characterized by positionally correlating or anti-correlating increases and decreases. The source of these elements may be the partitioning between the main phases (e.g., garnet–chlorite–biotite) or the breakdown of certain accessory phases (e.g., titanite in the garnet core, ilmenite in the garnet rim, or apatite with the transition to the garnet rim). However, this alone would not explain the positionally coincident oscillations of most of these elements. As discussed above regarding the inverse oscillatory distribution of Sc and V (Fig. 10h, i), this behavior could reflect fluctuating fO_2 caused by changes in the availability of the fluid matrix medium carrying the mentioned elements. In this case, with higher fluid availability, more Sc would enter the garnet structure along with Y + REE, with which it correlates well positionally, and vice versa for V. This process best fits the model of Konrad-Schmolke et al. (2023), which describes changes in fluid flows due to recurrent changes in

rock transport permeability. According to that model, permeability increases during ongoing dehydration reactions and decreases due to burial- or reaction-induced compaction with possible fluid drainage.

Atoll garnet formation

The process of atoll texture formation in garnet is widely debated, but the main mechanisms are thought to consist of: (1) partial dissolution/replacement of crystal inner parts and possibly also reprecipitation of garnet (Rast 1965; Smellie 1974; Homam 2003; Cheng et al. 2007; Galuskina et al. 2007; Faryad et al. 2010; Ruiz Cruz 2011; Jonnalagadda et al. 2017; Giuntoli et al. 2018; Kulhánek et al. 2021; Massonne and Li 2022); (2) multiple nucleation and coalescence (Spiess et al. 2001; Dobbs et al. 2003); (3) poikiloblastic enclosure of a high number of matrix phases that dominate one of the inner parts within the garnet grain (Atherton and Edmunds 1966; Ushakova and Usova 1990; Robyr et al. 2014; Godet et al. 2022); and (4) gradual coalescence of garnet in intergranular space of matrix phases (de Wit and Strong 1975). The high partition coefficient of Y + HREE during nucleation of garnet leads to the commonly observed peak of these elements in the garnet core. Considering the formation of atoll garnet by multiple nucleation and coalescence process (mechanism 2), it would be recognizable not only by major elements, especially the less diffusive Ca, but possibly also by the zoning of Y + HREE. However, the observed prograde concentric zoning with core-to-rim decreases of Y + HREE, even with local peaks in the rim part (Grt II) and with common idiomorphic Ca-zoning (Figs. 4, 7), does not support the formation of atoll garnet by either multiple nucleation and coalescence (mechanism 2) or gradual intergranular coalescence (mechanism 4). The poikiloblastic enclosure of matrix phases after garnet's bias in growth and its re-growth after enveloping matrix phases (mechanism 3) might form the observed prograde zoning without the need of dissolving inner parts of garnet. Such a mechanism would fit to the major element zoning distributions of some of the observed atoll garnets with Grt II forming only the rim part (Fig. 4b–e), but it does not explain the formation of common Grt II domains, in which islands and peninsulas replace Grt I from the inside of crystal (Figs. 4a, 7b, 8a). On the contrary, the dissolution and reprecipitation process (mechanism 1) might explain the missing parts of inner Grt I, commonly also replaced by Grt II. Considering the postulated controlling mechanism (1) of "dissolution and reprecipitation" in the genesis of the examined atoll garnets, which bears resemblance to that observed in atoll garnets from neighboring metabasites (Faryad et al. 2010; Kulhánek et al. 2021), there is a potential explanation for the observed micro-textures and compositional changes in garnet grains. To achieve a deeper understanding, a comprehensive exploration of the underlying origins and subsequent development of this proposed process, along with an investigation of the associated element transport mechanisms, was undertaken.

Since garnet constitutes the primary main phase into which Mn, Y, and HREE preferentially partition, the elevated concentrations of these elements are preserved in Grt I cores, but also in the Grt II on rim (forming the annular peak increase, Figs. 4, 7) or replacing Grt I in the central part (Fig. 8d). A possible source for the Grt II Y + HREE abundances might be the proposed Grt I dissolution, especially from the core parts. In this scenario, the Grt I would be during its dissolution replaced by Grt II growing inside atoll (forming islands and peninsulas of inner Grt II) or by other matrix phases which may then create a quartz + muscovite lagoon inside the atoll garnet. In contrast to the non-atoll garnets of sample JK22-20 (Fig. 10), the rim part (atoll Grt II) exhibits elevated peaks of Y and HREE accompanied by Na and Li in coupled substitution. Hence, it is unlikely that these substitutions involving Y and HREE would have occurred to such a significant extent in Grt II without sufficient source, such as the dissolution and subsequent release of these elements from Grt I.

In a previous study, (Kulhánek et al. 2021) the mass balance calculation in atoll garnet formation from the neighboring metabasites showed a release of Mn + Y + HREE but also some MREE from central Grt I during its dissolution, as well as their incorporation into Grt II on the rims or replacement of Grt I from inside along recognized microchannels. This was possible, thanks to the strong preference of Mn + Y + HREE to accommodate in garnet (Hollister 1966; Otamendi et al. 2002; Skora et al. 2006). The contents of Y + HREE, with the addition of Li, are also suitable to use for such mass balance calculation because of their low diffusion coefficients in comparison with the main elements of garnet, especially Mn (Chakraborty and Ganguly 1992; Tirone et al. 2005; Cahalan et al. 2014; Carlson et al. 2014).

To test the process of Grt I dissolution and transition of elements into concurrently growing Grt II, the mass balance calculation of Mn + Li + Y + REE between potentially dissolved parts of Grt I and stable Grt II, more specifically the multi-grain approach introduced in Kulhánek et al. (2021), was used. The Li contents were also measured and added to the mass balance calculation, owing to the generally good correlation observed between Li and Y + HREE distribution in the garnet maps and profiles (Figs. 4, 6, 7), which apparently results in this case from the coupled substitution of Li and Y + REE (Carlson et al. 2014). The multi-grain mass balance calculation involved a thorough analysis of 122 measurements from various parts of 31 garnet grains from sample F16-07, as presented in Fig. 8 and Supplementary Table 1S. These measurements were performed along transects (Fig. 8a) in carefully selected garnet parts to ensure the

representation of all zonal grains (Grt I, Grt II on the rim, and inner Grt II) in sufficient quantities. The objective was to compare the trace element contents of potentially dissolved Grt I and the current Grt II, relative to their volume percentages in the rock. To achieve this, arithmetic means (x) of elemental contents from Grt I, rim Grt II, and inner Grt II (islands and peninsulas in atoll), later used for mass balance, were calculated separately to facilitate a meaningful comparison. Notably, the abundances of Y + HREE in inner Grt II were significantly higher than in rim Grt II, leading to a separate calculation. This approach ensured that the arithmetic mean of trace elements in Grt II was not distorted, and that the standard deviation (SD) was not greater than the calculated arithmetic means (x) of the used elements (Table 3). Additionally, this finding also supports the assumption of an instantaneous transfer of Y + HREE during the dissolution of Grt I, which occurred in the core of the grain where Y + HREE abundances in Grt I were at their highest. The arithmetic means of (Li + Y + REE) values + MnO obtained separately for central Grt I, rim Grt II, and inner Grt II (Table 3) confirm the abundance of Li + Y + HREE and Ho, Dy, and Tb of MREE in central Grt I against rim Grt II. The inner Grt II (islands or peninsulas) shows values of Li and Y similar to those of Grt I and markedly higher arithmetic means of HREE, Ho, and Dy than those of Grt I (Table 3).

Another step for the mass balance calculation was to obtain the volumetric percentages of Grt I and II, which are present in the sample (referred as "residual Grt I" and "Grt II"), as well as Grt I, which was presumably already dissolved from the central parts of the garnet grains (referred as "projected dissolved Grt I"). The volume of residual Grt

Table 3 Calculated arithmetic means (x) and standard deviations (SD) of Li + Y + REE (ppm) and MnO (weight %) measured values of 122 spots for central Grt I, rim Grt II, and inner Grt II, as shown in Fig. 8

Element:	Nd	Sm	Eu	Gd	Tb	Dy	Ho	Er	Tm	Yb	Lu	Y	Li	MnO
Central Grt I (x)	0.13	0.58	0.73	7.37	3.88	43.22	10.81	31.28	4.20	25.26	3.03	295.85	29.31	0.92
Central Grt I (SD)	0.08	0.34	0.40	4.02	1.57	14.69	4.47	15.33	2.38	16.22	2.19	123.25	10.58	0.34
Rim Grt II (x)	0.16	1.32	1.39	12.18	3.14	19.01	3.52	9.46	1.32	8.88	1.32	93.60	12.99	0.70
Rim Grt II (SD)	0.04	0.27	0.26	2.40	0.90	6.15	1.14	2.98	0.41	2.73	0.46	30.07	3.77	0.13
Inner Grt II (x)	0.21	1.34	1.24	8.28	2.06	23.51	9.85	47.21	8.86	70.31	11.29	302.77	25.90	1.27
Inner Grt II (SD)	0.03	0.14	0.08	0.88	0.32	5.41	1.9	10.18	2.31	22.74	3.86	49.41	13.07	0.39

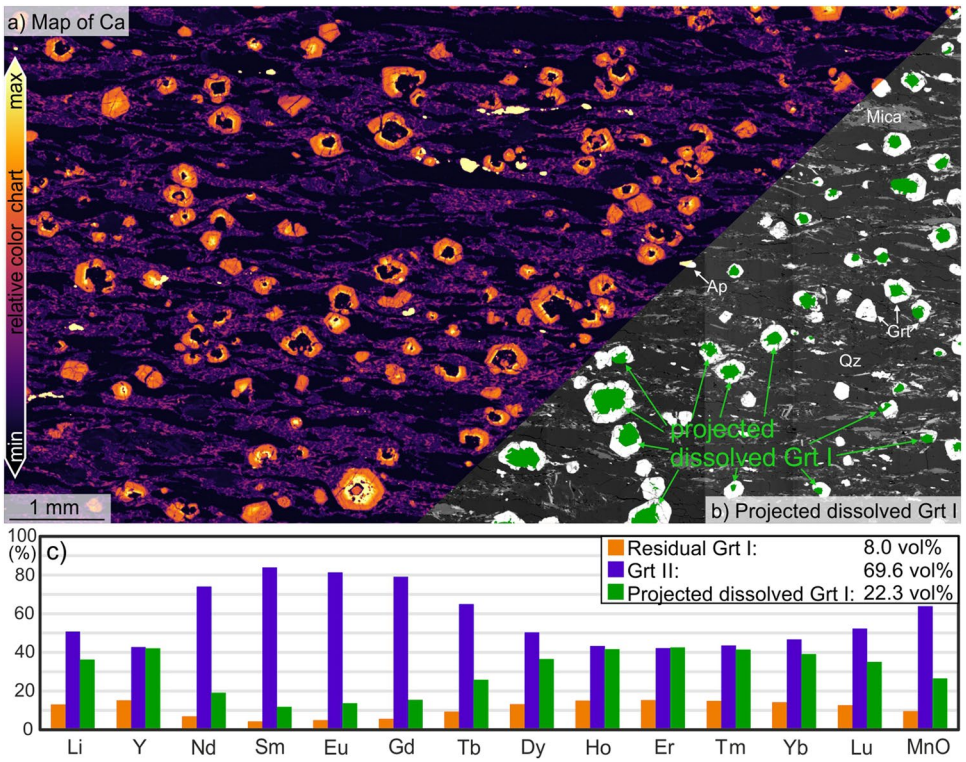

Fig. 11 Graphical presentation of the mass balance of MnO + Li + Y + REE between projected dissolved + residual Grt I and Grt II from a large-scale thin-section area (sample F16-07); **a** crosscut of the large-scale Ca-map, with visible orange to magenta Grt II parts and yellow residual Grt I inside rim Grt II, while the other bright yellow areas distributed in the matrix are phosphates; **b** crosscut of a large-scale BSE image with parts of projected dissolved garnets marked in green; **c** the MnO + Li + Y + REE percentage contents related to the vol% of residual Grt I, projected dissolved Grt I, and Grt II

I and Grt II was obtained by image analyses of relatively large-scale compositional maps (~ 10 × 10 mm), mainly Ca (crosscut on Fig. 11a), using the different colors of element concentrations and calculating the percentage representation of pixels of a given color by freely accessible GIMP software, version 2.10.8. The same method was also used to obtain a volumetric representation of projected dissolved Grt I, but it was necessary to first recognize the areas of Grt I projected dissolution inside the atolls based on the compositional maps and BSE images. These areas were then colored green on the grayscale BSE image to calculate the percentage of pixels corresponding to this presumably already missing Grt I (crosscut on Fig. 11b). The final part of the mass balance calculation consisted of the multiplication of obtained volumetric percentages of the garnet parts (normalized to 100%; listed in Fig. 11c) with the corresponding arithmetic means of MnO + Li + Y + REE in Grt I and II. The arithmetic mean contents of elements in the inner Grt II (islands or peninsulas) were multiplied with the corresponding volume of these inner parts and then added to the resulting Grt II values. The final resulting values of each element in the residual Grt I, Grt II, and projected dissolved Grt I were normalized to 100% to better compare their distribution in each garnet part, as shown in Fig. 11c.

The results of multi-grain mass balance show that more than two-thirds of the original modal volume of Grt I might have been dissolved and three times more of garnet (Grt II) was formed against this projected dissolved material (volumetric percentages in Fig. 11c). Grt II accommodates nearly identical amounts of Y, Ho, Er, Tm, and slightly more of Yb, compared to the volumes released from Grt I during its projected dissolution (Fig. 11c). The amount of Li, Dy, and Lu released from projected dissolved Grt I is approximately two-thirds of that in Grt II. An increasing enrichment from Tb to lighter REE is apparent in Grt II. The amount of MnO present in Grt II is twice as high as the amount released from projected dissolved Grt I, which may be due to the lowering of the original content by fast diffusion of Mn.

The calculated similar concentrations of Y, Ho, Er, and Tm, which were present in the presumably dissolved Grt I, to those detected in the current Grt II, might originate from the proposed dissolution of Grt I and transfer of these elements into concurrently growing Grt II. However, a slight increase in the abundances of Li, Dy, Yb, and Lu in Grt II is observed. This minor elevation of the heaviest REE (Yb and Lu) and possible co-substituent Li in Grt II can be attributed to the fact that the cores of Grt I, where the abundance of the heaviest REE is usually highest, have already been mostly dissolved and replaced in the rock. As a result, they could not be analyzed or included in the mass balance calculation, which may have slightly reduced the calculated Yb and Lu contents in Grt I. This observation is also supported by the fact that, in sample F16-07, the highest analyzed HREE contents are from the Grt II islands that replaced the very cores of Grt I. The elevated levels of Mn in Grt II (as mass balance result) may suggest a diffusely decreased original Mn bell-shaped distribution in Grt I. Moreover, notably higher concentrations of LREE and partly MREE in Grt II suggest that these elements also originated from sources beyond Grt I. One possible source for these elements among the observed accessory phases carrying higher amounts of MREE and LREE might be apatite (Fig. 8d; Table 2) with a plausible history of dissolution–reprecipitation along the PT path. The presence of larger rounded paragonite grains in sample F16-07 may suggest the potential decomposition of Na and MREE + LREE-bearing main phases, such as (Na-, Na-Ca-, Ca-) amphibole (Spandler et al. 2003; Konrad-Schmolke et al. 2008b) and Na-clinopyroxene (Kulhánek et al. 2021), followed by their replacement with paragonite and subsequent incorporation of released REE into Grt II. Apart from apatite and paragonite, other common sources of LREE and MREE in metamorphic phases could be the decomposition of minerals such as lawsonite, titanite, and epidote group minerals (Spandler et al. 2003; Konrad-Schmolke et al. 2008b; Volante et al. 2023). Despite the limitations associated with assessing the primary composition of whole Grt I, the mass balance calculation of Y + HREE indicates the possible transfer of these elements from the projected dissolved Grt I to the competitively formed Grt II. The result, thus, implies a partial dissolution and reprecipitation process for the formation of atoll garnet.

The replacement of Grt I may have occurred through microfractures that functioned as channels for elemental exchange. This assumption is based on the observation of microfractures in Grt I that are healed by garnet with a composition similar to Grt II, and by the growth of Grt II domains along them. This process may have been supported by fluids, as described for garnets in eclogites from studied region (Faryad et al. 2010; Collett et al. 2017; Kulhánek et al. 2021) and in HP rocks from other areas (Erambert and Austrheim 1993; Cheng et al. 2007; Konrad-Schmolke et al. 2007; Giuntoli et al. 2018; Bukała et al. 2020). The frequent occurrence of fluid inclusions in quartz lagoons within atoll garnets further suggests the involvement of fluids during the dissolution of central Grt I. Although the origin of fluids can be diverse in metamorphic process (e.g., Zelinková et al. 2022; Padrón-Navarta et al. 2023), the mass balance calculation points to the conclusion that the contribution of elements of interest from any potential external fluids is negligible. The presence of fluids, presumably derived from dehydration reactions, supports to some extent the transfer of Y and HREE from Grt I to Grt II, leading to the formation of an annular enrichment of these elements in Grt II.

Non-garnet trace element bearing phases

The principal minerals that likely served as significant sources of several trace elements during prograde metamorphism are phyllosilicates, notably chlorite and biotite. These minerals contain various elements such as Li, Ti, V, Cr, Co, Zn, Nb, Rb, and Sr (Fig. 6; Table 2). Additionally, biotite may contribute significantly to Sc (Yang et al. 1999), and chlorite might act as a considerable source of Y + REE (e.g., Konrad-Schmolke et al. 2008b). During HP prograde metamorphism, several other minerals act as significant sources of trace elements that migrate into garnet. This include mainly various amphibole group minerals (Li, Sc, Ti, V, Y, Nb, REE), lawsonite (Ti, Y, REE), epidote group minerals (Sc, V, Y, REE), titanite (Sc, Ti, Nb, Zr, Y, REE), and phosphates (Li, Y, REE), as referenced in Table 2 and other studies (e.g., Spandler et al. 2003; Konrad-Schmolke et al. 2008b; Kulhánek et al. 2021; Bebout et al. 2022; Volante et al. 2023).

During the retrogression of rock from HP conditions, trace elements from HP phases, including garnet, are released and incorporated into more stable metamorphic minerals. Consequently, during retrogression, the growth of the mentioned chlorite, biotite, and zoisite/allanite phases is stabilized. Additionally, staurolite is another observed retrograde phase carrying significant amounts of Li and Zn (Table 2).

Conclusion

Comprehensive quantitative analysis of trace elements has facilitated the identification of the formation mechanisms of different types of compositional zoning in garnet, atoll textures of garnet, and approximate pressure–temperature conditions during garnet growth. The main findings of this study can be summarized as follows.

(1) The formation process of atoll garnets, involving partial or complete dissolution of the inner part (Ca-rich Grt I) and subsequent reprecipitation of new garnet (Ca-poor Grt II) at the rim or in the inner part, was proposed based on detailed textural and compositional observations. The proposition of this process found support in the calculation of Y + HREE mass balance. The dissolution of Grt I is hypothesized to have been facilitated by fluids generated from dehydration reactions during prograde PT path. As a result of the projected dissolution of Grt I, rim Grt II exhibits annular increases in Ca, Mn, Y, HREE, as well as Li and Na through coupled substitution with Y, as these elements are incorporated due to their release from the dissolving Grt I. This proposed mechanism provides valuable insights into the intricate processes involved in the formation of atoll garnets and highlights the significance of mineral reactions and fluid-mediated reactions in metamorphic settings.

(2) The observed prograde growth of PT conditions of the rock samples to HP–MT aligns well with the compositional zoning patterns exhibited by the garnet, encompassing major and trace elements, as well as other minerals. The gradual increase in Co and Zn contents along the core-to-rim profile of the garnet indicates progressive increase of temperature conditions. The transition from overprint to annular zoning for elements such as Ti, Ca, Sm, Eu, Gd, and Tb, from the center to the rim of the grain, along with persistent overprint zoning for Cr throughout the entire grain, implies growth up to MT conditions. Moreover, the presence of coupled substitution of $^{VIII}(Na, Li)^{+} + {}^{IV}P^{5+}$ in the rim part of the grain provides evidence of potential HP–UHP conditions.

(3) The formation of annular zoning in elements is suggested to be influenced not only by the breakdown of main and accessory phases, resulting in the release and incorporation of elements into the growing garnet. Additionally, the presence of a fluid medium in the matrix, possibly derived from dehydration reactions, seems to play a significant role in controlling the extent and frequency of the observed annular variations in the garnet.

Supplementary Information The online version contains supplementary material available at https://doi.org/10.1007/s00410-023-02050-8.

Acknowledgements We extend our gratitude to the reviewers, D. R. Viete and an anonymous reviewer, for their valuable feedback, and to D. Rubatto for the meticulous editorial handling. Their constructive reviews have greatly contributed to the enhancement of this paper. This work was supported by the Czech Science Foundation (Grant No. 18-03160S), Grant Agency of Charles University (Grant No. 1194019), and by Charles University through the Cooperatio Program (Research Area GEOL) and Center for Geosphere Dynamics (UNCE/SCI/006). The authors wish to thank Geowriters for proofreading and language editing. We would like to express our sincere appreciation to M. Svojtka and J. Ďurišová for their assistance with LA-ICP-MS measurements, as well as to R. Jedlička for his contributions to EPMA measurements. Special thanks to O. Lexa for his assistance in data processing using Python, and to M. Racek for providing valuable insights in the field of trace element behavior.

Data availability The authors declare that the data supporting the findings of this study are available within the paper, and its supplementary information files.

Declarations

Conflict of interest The author declares that the submitted work does not bear any conflict of interest.

References

Ague JJ, Axler JA (2016) Interface coupled dissolution-reprecipitation in garnet from subducted granulites and ultrahigh-pressure rocks revealed by phosphorous, sodium, and titanium zonation. Am Mineral 101:1696–1699. https://doi.org/10.2138/am-2016-5707

Atherton MP, Edmunds WM (1966) An electron microprobe study of some zoned garnets from metamorphic rocks. Earth Planet Sci Lett 1:185–193. https://doi.org/10.1016/0012-821X(66)90066-5

Aygül M, Okay AI, Hacker BR, Kylander-Clark ARC (2022) REE behavior in warm and cold subducting oceanic crust. Int J Earth Sci 111:905–918. https://doi.org/10.1007/s00531-021-02156-z

Bebout GE, Ota T, Kunihiro T et al (2022) Lithium in garnet as a tracer of subduction zone metamorphic reactions: The record in ultra-high-pressure metapelites at Lago di Cignana, Italy. Geosphere 18:1020–1029. https://doi.org/10.1130/GES02473.1

Bell TH (1985) Deformation partitioning and porphyroblast rotation in meta-morphic rocks: a radical reinterpretation. J Metamorph Geol 3:109–118. https://doi.org/10.1111/j.1525-1314.1985.tb00309.x

Bell TH, Johnson SE (1989) Porphyroblast inclusion trails: the key to orogenesis. J Metamorph Geol 7:279–310. https://doi.org/10.1111/j.1525-1314.1989.tb00598.x

Bordage A, Brouder C, Balan E et al (2010) Electronic structure and local environment of substitutional V3+ in grossular garnet Ca3Al2(SiO4)3: K-edge X-ray absorption spectroscopy and first-principles modeling. Am Mineral 95:1161–1171. https://doi.org/10.2138/am.2010.3432

Boynton WV (1984) Cosmochemistry of the rare earth elements: meteorite studies. In: Henderson P (Ed) Rare Earth Element Geochemistry. Elsevier, pp 63–114

Brunet F, Bonneau V, Irifune T (2006) Complete solid-solution between Na3Al2 (PO4)3 and Mg3Al2 (SiO4)3 garnets at high pressure. Am Mineral 91:211–215. https://doi.org/10.2138/am.2006.2053

Bukała M, Barnes CJ, Jeanneret P et al (2020) Brittle deformation during eclogitization of early Paleozoic Blueschist. Front Earth Sci 8:1–17. https://doi.org/10.3389/feart.2020.594453

Cahalan RC, Kelly ED, Carlson WD (2014) Rates of Li diffusion in garnet: Coupled transport of Li and Y+REEs. Am Mineral 99:1676–1682. https://doi.org/10.2138/am.2014.4676

Canil D (2002) Vanadium in peridotites, mantle redox and tectonic environments: Archean to present. Earth Planet Sci Lett 195:75–90. https://doi.org/10.1016/S0012-821X(01)00582-9

Carlson WD (2012) Rates and mechanism of Y, REE, and Cr diffusion in garnet. Am Mineral 97:1598–1618. https://doi.org/10.2138/am.2012.4108

Carlson WD, Gale JD, Wright K (2014) Incorporation of Y and REEs in aluminosilicate garnet: Energetics from atomistic simulation. Am Mineral 99:1022–1034. https://doi.org/10.2138/am.2014.4720

Cave BJ, Stepanov AS, Large RR et al (2015) Release of trace elements through the sub-greenschist facies breakdown of detrital rutile to metamorphic titanite in the Otago Schist, New Zealand. Can Mineral 53:379–400. https://doi.org/10.3749/canmin.1400097

Chakraborty S, Ganguly J (1992) Cation diffusion in aluminosilicate garnets: experimental determination in spessartine-almandine diffusion couples, evaluation of effective binary diffusion coefficients, and applications. Contrib Mineral Petrol 111:74–86. https://doi.org/10.1007/BF00296579

Cheng H, Nakamura E, Kobayashi K, Zhou Z (2007) Origin of atoll garnets in eclogites and implications for the redistribution of trace elements during slab exhumation in a continental subduction zone. Am Mineral 92:1119–1129. https://doi.org/10.2138/am.2007.2343

Collett S, Štípská P, Kusbach V et al (2017) Dynamics of Saxothuringian subduction channel/wedge constrained by phase-equilibria modelling and micro-fabric analysis. J Metamorph Geol 35:253–280. https://doi.org/10.1111/jmg.12226

Collett S, Schulmann K, Štípská P, Míková J (2020) Chronological and geochemical constraints on the pre-variscan tectonic history of the Erzgebirge, Saxothuringian Zone. Gondwana Res 79:27–48. https://doi.org/10.1016/j.gr.2019.09.009

Dachs E, Proyer A (2002) Constraints on the duration of high-pressure metamorphism in the Tauern Window from diffusion modelling of discontinuous growth zones in eclogite garnet. J Metamorph Geol 20:769–780. https://doi.org/10.1046/j.1525-1314.2002.00404.x

de Wit MJ, Strong DF (1975) Eclogite-bearing amphibolites from the Appalachian mobile belt, northwest Newfoundland: dry versus wet metamorphism. J Geol 83:609–627. https://doi.org/10.1086/628144

Dempster TJ, La Piazza J, Taylor AG et al (2017) Chemical and textural equilibration of garnet during amphibolite facies metamorphism: The influence of coupled dissolution–reprecipitation. J Metamorph Geol 35:1111–1130. https://doi.org/10.1111/jmg.12278

Dempster TJ, Coleman S, Kennedy R et al (2020) Growth zoning of garnet porphyroblasts: grain boundary and microtopographic controls. J Metamorph Geol 38:1011–1027. https://doi.org/10.1111/jmg.12558

Dobbs HT, Peruzzo L, Seno F et al (2003) Unraveling the Schneeberg garnet puzzle: a numerical model of multiple nucleation and coalescence. Contrib Mineral Petrol 146:1–9. https://doi.org/10.1007/s00410-003-0488-4

Dziggel A, Wulff K, Kolb J et al (2009) Significance of oscillatory and bell-shaped growth zoning in hydrothermal garnet: evidence from the Navachab gold deposit, Namibia. Chem Geol 262:262–276. https://doi.org/10.1016/j.chemgeo.2009.01.027

Erambert M, Austrheim H (1993) The effect of fluid and deformation on zoning and inclusion patterns in poly-metamorphic garnets. Contrib Mineral Petrol 115:204–214. https://doi.org/10.1007/BF00321220

Faryad SW (2009) The Kutná Hora Complex (Moldanubian zone, Bohemian Massif): a composite of crustal and mantle rocks subducted to HP/UHP conditions. Lithos 109:193–208. https://doi.org/10.1016/j.lithos.2008.03.005

Faryad SW (2011) Distribution and geological position of high-/ultra-high-pressure units within the European Variscan Belt. In: Dobrzhinetskaya L, Faryad SW, Wallis S, Cuthbert S (eds) Ultrahigh pressure metamorphism: 25 years after The Discovery Of Coesite And Diamond. Elsevier, pp 361–397

Faryad SW (2012) High-pressure polymetamorphic garnet growth in eclogites from the Mariánské Lázně Complex (Bohemian Massif). Eur J Mineral 24:483–497. https://doi.org/10.1127/0935-1221/2012/0024-2184

Faryad SW, Cuthbert SJ (2020) High-temperature overprint in (U)HPM rocks exhumed from subduction zones; A product of isothermal decompression or a consequence of slab break-off (slab roll-back)? Earth-Sci Rev 202:1–14. https://doi.org/10.1016/j.earscirev.2020.103108

Faryad SW, Ježek J (2019) Compositional zoning in garnet and its modification by diffusion during pressure and temperature changes in metamorphic rocks; an approach and software. Lithos 332–333:287–295. https://doi.org/10.1016/j.lithos.2019.03.002

Faryad SW, Kachlík V (2013) New evidence of blueschist facies rocks and their geotectonic implication for Variscan suture(s) in the Bohemian Massif. J Metamorph Geol 31:63–82. https://doi.org/10.1111/jmg.12009

Faryad SW, Klápová H, Nosál L (2010) Mechanism of formation of atoll garnet during high-pressure metamorphism. Mineral Mag 74:111–126. https://doi.org/10.1180/minmag.2010.074.1.111

Faryad SW, Baldwin SL, Jedlicka R, Ježek J (2019) Two-stage garnet growth in coesite eclogite from the southeastern Papua New Guinea (U)HP terrane and its geodynamic significance. Contrib Mineral Petrol 174:73. https://doi.org/10.1007/s00410-019-1612-4

Faryad SW, Ježek J, Connolly JAD (2022a) Advantages and limitations of combined diffusion-phase equilibrium modelling for pressure–temperature–time history of metamorphic rocks. J Petrol 63:1–19. https://doi.org/10.1093/petrology/egac118

Faryad SW, Ježek J, Kulhánek J (2022b) Constraining the P-T path of (U)HP rocks with reaction overstepping during subduction; example from the Western Gneiss Region (Norway). J Metamorph Geol 40:1427–1446. https://doi.org/10.1111/jmg.12680

Franke W (2000) The mid-European segment of the Variscides: Tectonostratigraphic units, terrane boundaries and plate tectonic evolution. In: Franke W, Haak V, Oncken O, Tanner D (eds) Orogenic Processes: Quantification and Modelling in the Varicsan Belt. Geological Society, London, Special Publications, pp 35–56

Gaidies F, Morneau YE, Petts DC et al (2021) Major and trace element mapping of garnet: Unravelling the conditions, timing and rates of metamorphism of the Snowcap assemblage, west-central Yukon. J Metamorph Geol 39:133–164. https://doi.org/10.1111/jmg.12562

Galuskina I, Galuskin E, Włodyka R et al (2007) Atoll garnets in "achtarandite" serpentinites: Morphology, composition and mode of origin. Mineral Pol 38:139–149. https://doi.org/10.2478/v10002-007-0022-9

Garber JM, Hacker BR, Kylander-Clark ARC et al (2017) Controls on trace element uptake in metamorphic titanite: Implications for petrochronology. J Petrol 58:1031–1057. https://doi.org/10.1093/petrology/egx046

George FR, Gaidies F, Boucher B (2018) Population-wide garnet growth zoning revealed by LA-ICP-MS mapping: implications for trace element equilibration and syn-kinematic deformation during crystallisation. Contrib to Mineral Petrol 173:1–22. https://doi.org/10.1007/s00410-018-1503-0

Giuntoli F, Lanari P, Engi M (2018) Deeply subducted continental fragments - Part 1: fracturing, dissolution-precipitation, and diffusion processes recorded by garnet textures of the central Sesia Zone (western Italian Alps). Solid Earth 9:167–189. https://doi.org/10.5194/se-9-167-2018

Godet A, Raimondo T, Guilmette C (2022) Atoll garnet: insights from LA-ICP-MS trace element mapping. Contrib Mineral Petrol 177:1–15. https://doi.org/10.1007/s00410-022-01924-7

Goncalves P, Raimondo T, Paquette J, de Souza S, de Oliveira J (2021) Garnet as a monitor for melt–rock interaction: Textural, mineralogical, and compositional evidence of partial melting and melt-driven metasomatism. J Metamorph Geol 39:617–648. https://doi.org/10.1111/jmg.12592

Grew ES, Locock AJ, Mills SJ et al (2013) IMA report: Nomenclature of the garnet supergroup. Am Mineral 98:785–810. https://doi.org/10.2138/am.2013.4201

Haifler J, Kotková J (2016) UHP-UHT peak conditions and near-adiabatic exhumation path of diamond-bearing garnet-clinopyroxene rocks from the Eger Crystalline Complex, North Bohemian Massif. Lithos 248–251:366–381. https://doi.org/10.1016/j.lithos.2016.02.001

Hajná J, Žák J, Kachlík V (2011) Structure and stratigraphy of the Teplá-Barrandian Neoproterozoic, Bohemian Massif: a new plate-tectonic reinterpretation. Gondwana Res 19:495–508. https://doi.org/10.1016/j.gr.2010.08.003

Hanrahan M, Brey G, Woodland A et al (2009a) Towards a Li barometer for bimineralic eclogites: experiments in CMAS. Contrib to Mineral Petrol 158:169–183. https://doi.org/10.1007/s00410-009-0376-7

Hanrahan M, Brey G, Woodland A et al (2009b) Li as a barometer for bimineralic eclogites: experiments in natural systems. Lithos 112:992–1001. https://doi.org/10.1016/j.lithos.2009.05.021

Hermann J, Spandler CJ (2008) Sediment melts at sub-arc depths: an experimental study. J Petrol 49:717–740. https://doi.org/10.1093/petrology/egm073

Hickey KA, Bell TH (1999) Behaviour of rigid objects during deformation and metamorphism: a test using schists from the Bolton syncline, Connecticut, USA. J Metamorph Geol 17:211–228. https://doi.org/10.1046/j.1525-1314.1999.00192.x

Hollister LS (1966) Garnet zoning: an interpretation based on the rayleigh fractionation model. Science (80-) 154:1647–1651. https://doi.org/10.1126/science.154.3757.1647

Holub FV, Souček J (1992) Blueschist-greenschist metamorphism of metabasites in the western Krušné Hory (Erzgebirge) Mts. Zentralblatt für Geol und Paläontologie, Tl 1 7/8:815–826

Homam SM (2003) Formation of atoll garnet in the ardara aureole, NW Ireland. J Sci Islam Repub Iran 14:247–258

Jaffe HW (1951) The role of yttrium and other minor elements in the garnet group. Am Mineral 36:133–155

Jamtveit B, Wogelius RA, Fraser DG (1993) Zonation patterns of skarn garnets: records of hydrothermal system evolution. Geology 21:113–116. https://doi.org/10.1130/0091-7613(1993)021%3c0113:ZPOSGR%3e2.3.CO;2

Jastrzębski M, Żelaźniewcz A, Sláma J et al (2021) Provenance of Precambrian basement of the Brunovistulian Terrane: New data from its Silesian part (Czech Republic, Poland), central Europe, and implications for Gondwana break-up. Precambrian Res 355:1–17. https://doi.org/10.1016/j.precamres.2021.106108

Jedlicka R, Faryad SW, Hauzenberger C (2015) Prograde metamorphic history of UHP granulites from the moldanubian zone (Bohemian Massif) revealed by major element and Y + REE zoning in garnets. J Petrol 56:2069–2088. https://doi.org/10.1093/petrology/egv066

Jeřábek P, Konopásek J, Žáčková E (2016) Two-stage exhumation of subducted Saxothuringian continental crust records underplating in the subduction channel and collisional forced folding (Krkonoše-Jizera Mts., Bohemian Massif). J Str Geol 89:214–229. https://doi.org/10.1016/j.jsg.2016.06.008

Jochum KP, Weis U, Stoll B et al (2011) Determination of reference values for NIST SRM 610–617 glasses following ISO guidelines. Geostand Geoanalytical Res 35:397–429. https://doi.org/10.1111/j.1751-908X.2011.00120.x

Jonnalagadda MK, Karmalkar NR, Duraiswami RA et al (2017) Formation of atoll garnets in the UHP eclogites of the Tso Morari Complex, Ladakh, Himalaya. J Earth Syst Sci 126:1–23. https://doi.org/10.1007/s12040-017-0887-y

Jouvent M, Lexa O, Peřestý V, Jeřábek P (2022) New constraints on the tectonometamorphic evolution of the Erzgebirge orogenic wedge (Saxothuringian Domain, Bohemian Massif). J Metamorph Geol 40:687–715. https://doi.org/10.1111/jmg.12643

Jouvent M, Peřestý V, Jeřábek P et al (2023) Assembly of the Variscan Orogenic Wedge in the Bohemian Massif: Monazite U-Pb Geochronology of the Tectonic Events Recorded in Saxothuringian Metasediments. Tectonics 42:1–29. https://doi.org/10.1029/2022TC007626

Klápová H (1990) Eclogites of the Bohemian part of the Saxothuringicum. Academia, Prague

Klápová H, Konopásek J, Schulmann K (1998) Eclogites from the Czech part of the Erzgebirge: multi-stage metamorphic and structural evolution. J Geol Soc London 155:567–583. https://doi.org/10.1144/gsjgs.155.3.0567

Kobayashi T, Hirajima T, Hiroi Y, Svojtka M (2008) Determination of SiO2 raman spectrum indicating the transformation from coesite to quartz in Gföhl migmatitic gneisses in the Moldanubian Zone,

Czech Republic. J Mineral Petrol Sci 103:105–111. https://doi.org/10.2465/jmps.071020
Kohn MJ (2017) Titanite Petrochronology. Rev Mineral. Geochemistry 83:419–441. https://doi.org/10.2138/rmg.2017.83.13
Konopásek J (1998) Formation and destabilization of the high pressure assemblage garnet-phengite-paragonite (Krusne hory Mountains, Bohemian Massif): The significance of the Tschermak substitution in the metamorphism of pelitic rocks. Lithos 42:269–284. https://doi.org/10.1016/S0024-4937(97)00046-7
Konopásek J (2001) Eclogitic micaschists in the central part of the Krušné hory Mountains (Bohemian Massif). Eur J Mineral 13:87–100. https://doi.org/10.1127/0935-1221/01/0013-0087
Konopásek J, Schulmann K (2005) Contrasting Early Carboniferous field geotherms: evidence for accretion of a thickened orogenic root and subducted Saxothuringian crust (Central European Variscides). J Geol Soc London 162:463–470. https://doi.org/10.1144/0016-764904-004
Konopásek J, Schulmann K, Lexa O (2001) Structural evolution of the central part of the Krušné hory (Erzgebirge) Mountains in the Czech Republic-evidence for changing stress regime during Variscan compression. J Str Geol 23:1373–1392. https://doi.org/10.1016/S0191-8141(01)00003-7
Konopásek J, Anczkiewicz R, Ábek PJ et al (2019) Chronology of the saxothuringian subduction in the west sudetes (Bohemian massif, Czech Republic and Poland). J Geol Soc London 176:492–504. https://doi.org/10.1144/jgs2018-173
Konrad-Schmolke M, Babist J, Handy MR, O'Brien PJ (2006) The physico-chemical properties of a subducted slab from garnet zonation patterns (Sesia Zone, Western Alps). J Petrol 47:2123–2148. https://doi.org/10.1093/petrology/egl039
Konrad-Schmolke M, O'Brien PJ, Heidelbach F (2007) Compositional re-equilibration of garnet: the importance of sub-grain boundaries. Eur J Mineral 19:431–438. https://doi.org/10.1127/0935-1221/2007/0019-1749
Konrad-Schmolke M, O'Brien PJ, de Capitani C, Carswell DA (2008a) Garnet growth at high- and ultra-high pressure conditions and the effect of element fractionation on mineral modes and composition. Lithos 103:309–332. https://doi.org/10.1016/j.lithos.2007.10.007
Konrad-Schmolke M, Zack T, O'Brien PJ, Jacob DE (2008b) Combined thermodynamic and rare earth element modelling of garnet growth during subduction: Examples from ultrahigh-pressure eclogite of the Western Gneiss Region, Norway. Earth Planet Sci Lett 272:488–498. https://doi.org/10.1016/j.epsl.2008.05.018
Konrad-Schmolke M, Halama R, Chew D et al (2023) Discrimination of thermodynamic and kinetic contributions to the heavy rare earth element patterns in metamorphic garnet. J Metamorph Geol 41:465–490. https://doi.org/10.1111/jmg.12703
Konzett J, Frost DJ (2009) The high P-T stability of hydroxyl-apatite in natural and simplified MORB - An experimental study to 15 GPa with implications for transport and storage of phosphorus and halogens in subduction zones. J Petrol 50:2043–2062. https://doi.org/10.1093/petrology/egp068
Kotková J, Janák M (2015) UHP kyanite eclogite associated with garnet peridotite and diamond-bearing granulite, northern Bohemian Massif. Lithos 226:255–264. https://doi.org/10.1016/j.lithos.2015.01.016
Kotková J, O'Brien PJ, Ziemann MA (2011) Diamond and coesite discovered in Saxony-type granulite: Solution to the Variscan garnet peridotite enigma. Geology 39:667–670. https://doi.org/10.1130/G31971.1
Kröner A, Willner AP, Hegner E et al (1995) Latest precambrian (Cadomian) zircon ages, Nd isotopic systematics and P-T evolution of granitoid orthogneisses of the Erzgebirge, Saxony and Czech Republic. Geol Rundschau 84:437–456. https://doi.org/10.1007/BF00284512
Kroner U, Hahn T, Romer RL, Linnemann U (2007) The variscan orogeny in the saxo-thuringian zone - Heterogenous overprint of Cadomian/Paleozoic Peri-Gondwana crust. Spec Pap Geol Soc Am 423:153–172. https://doi.org/10.1130/2007.2423(06)
Kryl J, Jeřábek P, Lexa O (2021) From subduction channel to orogenic wedge: Exhumation recorded by orthogneiss microstructures in Erzgebirge, Bohemian Massif. Tectonophysics 820:1–19. https://doi.org/10.1016/j.tecto.2021.229096
Kulhánek J, Faryad SW, Jedlicka R, Svojtka M (2021) Dissolution and reprecipitation of garnet during eclogite facies metamorphism; major and trace elements transfer during atoll garnet formation. J Petrol 62:1–22. https://doi.org/10.1093/petrology/egab077
Lanzirotti A (1995) Yttrium zoning in metamorphic garnets. Geochim Cosmochim Acta 59:4105–4110. https://doi.org/10.1016/0016-7037(95)00320-Y
Likhanov II (2019) Mass-transfer and differential element mobility in metapelites during multistage metamorphism of the Yenisey Ridge, Siberia. Geol Soc London Spec Publ 478:89–115. https://doi.org/10.1144/SP478.11
Maierová P, Schulmann K, Štípská P et al (2021) Trans-lithospheric diapirism explains the presence of ultra-high pressure rocks in the European Variscides. Commun Earth Environ 2:1–9. https://doi.org/10.1038/s43247-021-00122-w
Massonne H-J (2001) First find of coesite in the ultrahigh-pressure metamorphic area of the central Erzgebirge, Germany. Eur J Mineral 13:565–570. https://doi.org/10.1127/0935-1221/2001/0013-0565
Massonne H-J, Kopp J (2005) A low-variance mineral assemblage with talc and phengite in an eclogite from the Saxonian Erzgebirge, central Europe, and its P-T evolution. J Petrol 46:355–375. https://doi.org/10.1093/petrology/egh079
Massonne H-J, Nasdala L (2003) Characterization of an early metamorphic stage through inclusions in zircon of a diamon-diferous quartzofeldspathic rock from the Erzgebirge, Germany. Am Mineral 88:883–889. https://doi.org/10.2138/am-2003-5-618
Massonne H-J, O'Brien PJ (2003) The Bohemian Massif and the NW Himalaya. In: Carswel DA, Compagnoni R (eds) Ultrahigh Pressure Metamorphism. Eotvos University Press, Budapest, pp 145–187
Massonne H-J, Li B (2022) Eclogite with unusual atoll garnet from the southern Armorican Massif, France: Pressure-temperature path and geodynamic implications. Tectonophysics 823:229183. https://doi.org/10.1016/j.tecto.2021.229183
Medaris LG, Ghent ED, Wang HF et al (2006) The Spačice eclogite: Constraints on the P-T-t history of the Gföhl granulite terrane, Moldanubian Zone, Bohemian Massif. Mineral Petrol 86:203–220. https://doi.org/10.1007/s00710-005-0095-3
Mingram B (1998) The Erzgebirge, Germany, a subducted part of northern Gondwana: Geochemical evidence for repetition of early Palaeozoic metasedimentary sequences in metamorphic thrust units. Geol Mag 135:785–801. https://doi.org/10.1017/S0016756898001769
Moore SJ, Carlson WD, Hesse MA (2013) Origins of yttrium and rare earth element distributions in metamorphic garnet. J Metamorph Geol 31:663–689. https://doi.org/10.1111/jmg.12039
Nasdala L, Massonne H-J (2000) Microdiamonds from the Saxonian Erzgebirge, Germany : in situ micro-Raman characterisation. Eur J Mineral 12:495–498. https://doi.org/10.1127/0935-1221/2000/0012-0495
Oberti R, Quartieri S, Dalconi MC et al (2006) Site preference and local geometry of Sc in garnets: Part I. Multifarious mechanisms in the pyrope-grossular join. Am Mineral 91:1230–1239. https://doi.org/10.2138/am.2006.2037
Otamendi JE, de la Rosa JD, Patiño Douce AE, Castro A (2002) Rayleigh fractionation of heavy rare earths and yttrium during metamorphic garnet growth. Geology 30:159–162. https://doi.org/10.1130/0091-7613(2002)030%3c0159:RFOHRE%3e2.0.CO;2

Padrón-Navarta JA, López Sánchez-Vizcaíno V, Menzel MD et al (2023) Mantle wedge oxidation from deserpentinization modulated by sediment-derived fluids. Nat Geosci 16:268–275. https://doi.org/10.1038/s41561-023-01127-0

Passchier CW, Trouw RAJ, Zwart HJ, Vissers RLM (1992) Porphyroblast rotation: eppur si muove? J Metamorph Geol 10:283–294. https://doi.org/10.1111/j.1525-1314.1992.tb00083.x

Peřestý V, Lexa O, Holder R et al (2017) Metamorphic inheritance of Rheic passive margin evolution and its early-Variscan overprint in the Teplá-Barrandian Unit, Bohemian Massif. J Metamorph Geol 35:327–355. https://doi.org/10.1111/jmg.12234

Peřestý V, Lexa O, Jeřábek P (2020) Restoration of early-Variscan structures exposed along the Teplá shear zone in the Bohemian Massif: constraints from kinematic modelling. Int J Earth Sci 109:1189–1211. https://doi.org/10.1007/s00531-019-01806-7

Perraki M, Faryad SW (2014) First finding of microdiamond, coesite and other UHP phases in felsic granulites in the Moldanubian Zone: Implications for deep subduction and a revised geodynamic model for Variscan Orogeny in the Bohemian Massif. Lithos 202–203:157–166. https://doi.org/10.1016/j.lithos.2014.05.025

Pyle JM, Spear FS (1999) Yttrium zoning in garnet: Coupling of major and accessory phases during metamorphic reactions. Geol Mater Res 1:1–49

Quartieri S, Oberti R, Boiocchi M et al (2006) Site preference and local geometry of Sc in garnets: Part II. The crystal-chemistry of octahedral Sc in the andradite - Ca3Sc2Si3O12 join. Am Mineral 91:1240–1248. https://doi.org/10.2138/am.2006.2038

Raimondo T, Payne J, Wade B et al (2017) Trace element mapping by LA-ICP-MS: assessing geochemical mobility in garnet. Contrib Mineral Petrol 172:1–22. https://doi.org/10.1007/s00410-017-1339-z

Rast N (1965) Nucleation and growth of metamorphic minerals. In: Pitcher WS, Flinn GW (eds) Controls of Metamorphism. Oliver and Boyd, Edinburgh, pp 73–102

Righter K, Sutton S, Danielson L et al (2011) The effect of fO2 on the partitioning and valence of v and Cr in garnet/melt pairs and the relation to terrestrial mantle v and Cr content. Am Mineral 96:1278–1290. https://doi.org/10.2138/am.2011.3690

Ringwood AE, Major A (1971) Synthesis of majorite and other high pressure garnets and perovskites. Earth Planet Sci Lett 12:411–418. https://doi.org/10.1016/0012-821X(71)90026-4

Robyr M, Darbellay B, Baumgartner LP (2014) Matrix-dependent garnet growth in polymetamorphic rocks of the Sesia zone, Italian Alps. J Metamorph Geol 32:3–24. https://doi.org/10.1111/jmg.12055

Rötzler K, Schumacher R, Maresch WV, Willner AP (1998) Characterization and geodynamic implications of contrasting metamorphic evolution in juxtaposed high-pressure units of the western Erzgebirge (Saxony, Germany). Eur J Mineral 10:261–280. https://doi.org/10.1127/ejm/10/2/0261

Rötzler K (1995) Die PT-Entwicklung der Metamorphite des Mittel- und Westerzgebirges. GeoForschungsZentrum Potsdam, Potsdam

Rubatto D, Burger M, Lanari P et al (2020) Identification of growth mechanisms in metamorphic garnet by high-resolution trace element mapping with LA-ICP-TOFMS. Contrib Mineral Petrol 175:1–19. https://doi.org/10.1007/s00410-020-01700-5

Ruiz Cruz MD (2011) Origin of atoll garnet in schists from the Alpujárride complex (central zone of the Betic Cordillera, Spain): Implications on the P-T evolution. Mineral Petrol 101:245–261. https://doi.org/10.1007/s00710-011-0147-9

Schäfer J, Neuroth H, Ahrendt H et al (1997) Accretion and exhumation at a Variscan active margin, recorded in the Saxothuringian flysch. Geol Rundschau 86:599–611. https://doi.org/10.1007/s005310050166

Schertl HP, Schreyer W, Chopin C (1991) The pyrope-coesite rocks and their country rocks at Parigi, Dora Maira Massif, Western Alps: detailed petrography, mineral chemistry and PT-path. Contrib Mineral Petrol 108:1–21. https://doi.org/10.1007/BF00307322

Schmädicke E, Okrusch M, Schmidt W (1992) Eclogite-facies rocks in the Saxonian Erzgebirge, Germany: high pressure metamorphism under contrasting P-T conditions. Contrib Mineral Petrol 110:226–241. https://doi.org/10.1007/BF00310740

Schoneveld C (1977) A study of some typical inclusion patterns in strongly paracrystalline-rotated garnets. Tectonophysics 39:453–471. https://doi.org/10.1016/0040-1951(77)90109-3

Schulmann K, Konopásek J, Janoušek V et al (2009) An Andean type Palaeozoic convergence in the Bohemian Massif. Comptes Rendus - Geosci 341:266–286. https://doi.org/10.1016/j.crte.2008.12.006

Schulmann K, Lexa O, Janoušek V et al (2014) Anatomy of a diffuse cryptic suture zone: An example from the Bohemian Massif, European variscides. Geology 42:275–278. https://doi.org/10.1130/G35290.1

Skora S, Baumgartner LP, Mahlen NJ et al (2006) Diffusion-limited REE uptake by eclogite garnets and its consequences for Lu-Hf and Sm-Nd geochronology. Contrib Mineral Petrol 152:703–720. https://doi.org/10.1007/s00410-006-0128-x

Smellie J (1974) Formation of Atoll Garnets from the Aureole of the Ardara Pluton, Co., Donegal, Ireland. Mineral Mag 39:878–888. https://doi.org/10.1180/minmag.1974.039.308.07

Spandler C, Hermann J, Arculus R, Mavrogenes J (2003) Redistribution of trace elements during prograde metamorphism from lawsonite blueschist to eclogite facies; implications for deep subduction-zone processes. Contrib Mineral Petrol 146:205–222. https://doi.org/10.1007/s00410-003-0495-5

Spiess R, Peruzzo L, Prior DJ, Wheeler J (2001) Development of garnet porphyroblasts by multiple nucleation, coalescence and boundary driven rotations. J Metamorph Geol 19:269–290. https://doi.org/10.1046/j.0263-4929.2000.00311.x

Thompson RN (1975) Is upper-mantle phosphorus contained in sodic garnet? Earth Planet Sci Lett 26:417–424. https://doi.org/10.1016/0012-821X(75)90017-5

Tirone M, Ganguly J, Dohmen R et al (2005) Rare earth diffusion kinetics in garnet: Experimental studies and applications. Geochim Cosmochim Acta 69:2385–2398. https://doi.org/10.1016/j.gca.2004.09.025

Ushakova EN, Usova LV (1990) Atoll garnets in a contact aureole of one of the region of the South-Eastern Tuva. Geol i Geofiz 4:50–59

van Achterbergh E, Ryan CG, Jackson SE, Griffin WL (2001) Data reduction software for LA-ICP- MS. In: Sylvester PJ (Ed) Laser ablation-ICP-mass spectrometry in the Earth Sciences: Principles and applications. Mineralogical Association of Canada, Short Course Series, Ottawa, pp 239–243

van Achterbergh E, Ryan CG, Griffin W (2005) Glitter! Gemoc National Key Centre McQuarie University, Australia, User's manual. On-line interactive data reduction for the LA-ICPMS microprobe

van Westrenen W, Blundy J, Wood B (1999) Crystal-chemical controls on trace element partitioning between garnet and anhydrous silicate melt. Am Mineral 84:838–847. https://doi.org/10.2138/am-1999-5-617

van Westrenen W, Allan NL, Blundy JD et al (2000) Atomistic simulation of trace element incorporation into garnets-comparison with experimental garnet-melt partitioning data. Geochim Cosmochim Acta 64:1629–1639. https://doi.org/10.1016/S0016-7037(00)00336-7

Vance D, O'Nions RK (1990) Isotopic chronometry of zoned garnets: growth kinetics and metamorphic histories. Earth Planet Sci Lett 97:227–240. https://doi.org/10.1016/0012-821X(90)90044-X

Viete DR, Hacker BR, Allen MB et al (2018) Metamorphic records of multiple seismic cycles during subduction. Sci Adv 4:1–14. https://doi.org/10.1126/sciadv.aaq0234

Volante S, Blereau E, Guitreau M et al (2023) Current applications using key mineral phases in igneous and metamorphic geology: perspectives for the future. Geol Soc London, Spec Publ 537:1–65. https://doi.org/10.1144/SP537-2022-254

Warr LN (2021) IMA–CNMNC approved mineral symbols. Mineral Mag 85:291–320. https://doi.org/10.1180/mgm.2021.43

Williamson WO (1934) The composite gneiss and contaminated granodiorite of Glen Shee, Pertshire. Q J Geol Soc 91:382–422. https://doi.org/10.1144/GSL.JGS.1935.091.01-04.14

Willner AP, Rötzler K, Maresch WV (1997) Pressure-temperature and fluid evolution of Quartzo-Feldspathic metamorphic rocks with a relic high-pressure, Granulite-Facies History from the Central Erzgebirge (Saxony, Germany). J Petrol 38:307–336. https://doi.org/10.1093/petroj/38.3.307

Willner AP, Krohe A, Maresch WV (2000) Interrelated P-T-t-d Paths in the Variscan Erzgebirge Dome (Saxony, Germany): Constraints on the Rapid Exhumation of High-Pressure Rocks from the Root Zone of a Collisional Orogen. Int Geol Rev 42:64–85. https://doi.org/10.1080/00206810009465070

Willner AP, Sebazungu E, Gerya TV et al (2002) Numerical modelling of PT-paths related to rapid exhumation of high-pressure rocks from the crustal root in the Variscan Erzgebirge Dome (Saxony/Germany). J Geodyn 33:281–314. https://doi.org/10.1016/S0264-3707(01)00071-0

Yang P, Pattison D (2006) Genesis of monazite and Y zoning in garnet from the Black Hills, South Dakota. Lithos 88:233–253. https://doi.org/10.1016/j.lithos.2005.08.012

Yang P, Rivers T (2001) Chromium and manganese zoning in pelitic garnet and kyanite: Spiral, overprint, and oscillatory (?) zoning patterns and the role of growth rate. J Metamorph Geol 19:455–474. https://doi.org/10.1046/j.0263-4929.2001.00323.x

Yang P, Rivers T (2002) The origin of Mn and Y annuli in garnet and the thermal dependence of P in garnet and Y in apatite in calc-pelite and pelite, Gagnon terrane, western Labrador. Geol Mater Res 4:1–35

Yang P, Rivers T, Jackson S (1999) Crystal-chemical and thermal controls on trace-element partitioning between coexisting garnet and biotite in metamorphic rocks from western Labrador. Can Mineral 37:443–468

Ye K, Cong B, Ye D (2000) The possible subduction of continental material to depths greater than 200 km. Nature 407:734–736. https://doi.org/10.1038/35037566

Závada P, Schulmann K, Racek M et al (2018) Role of strain localization and melt flow on exhumation of deeply subducted continental crust. Lithosphere 10:217–238. https://doi.org/10.1130/L666.1

Závada P, Štípská P, Hasalová P et al (2021) Monazite geochronology in melt-percolated UHP meta-granitoids: An example from the Erzgebirge continental subduction wedge, Bohemian Massif. Chem Geol 559:1–19. https://doi.org/10.1016/j.chemgeo.2020.119919

Zelinková T, Racek M, Abart R (2022) Compositional trends in Ba-, Ti-, and Cl-rich micas from metasomatized mantle rocks of the Gföhl Unit, Bohemian Massif, Austria. Am Mineral. https://doi.org/10.2138/am-2022-8746 (**in press**)

Zhu L, Chen RX, Zheng YF et al (2022) Multistage growth of garnet fingerprints the behavior and property of metamorphic fluids in a Paleotethyan oceanic subduction zone. Lithos 430–431:1–23. https://doi.org/10.1016/j.lithos.2022.106851